Dual carbonate clumped isotopes (Δ_{47}-Δ_{48}) constrains kinetic effects and timescales in peridotite-associated springs at The Cedars, Northern California

Zeeshan A. Parvez[a, b, c,*], Jamie K. Lucarelli[a,b,*], Irvin W. Matamoros[a, b], Joshua Rubi[b, d], Kevin Miguel[b, d], Ben Elliott[a, b], Randy Flores[a, b], Robert N. Ulrich[a, b], Robert A. Eagle[b, e, f], James M. Watkins[g], John N. Christensen[h], Aradhna Tripati[a, b, e, f]

[a] *Department of Earth, Planetary, and Space Sciences, University of California, Los Angeles, CA, USA*
[b] *Center for Diversity and Leadership in Science, University of California, Los Angeles, CA, USA*
[c] *Department of Chemistry and Biochemistry, University of California, Los Angeles, CA, USA*
[d] *East Los Angeles College, Los Angeles, CA, USA*
[e] *Department of Atmospheric and Oceanic Sciences, University of California, Los Angeles, CA, USA*
[f] *Institute of Environment and Sustainability, University of California, Los Angeles, CA, USA*
[g] *Department of Earth Sciences, University of Oregon, Eugene, OR, USA*
[h] *Department of Energy Geosciences, Lawrence Berkeley National Laboratory, Berkeley CA, USA*
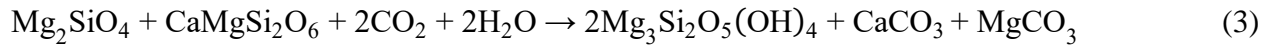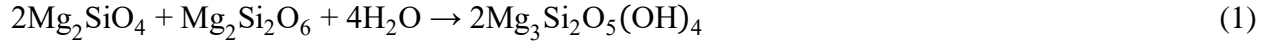
* Joint first author.

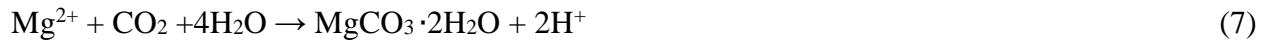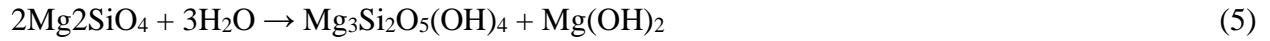Corresponding author: Aradhna Tripati, atripati@g.ucla.edu

Abstract

The Cedars is an area in Northern California with a chain of highly alkaline springs resulting from CO_2-charged meteorological water interacting with a peridotite body. Serpentinization resulting from this interaction at depth leads to the sequestration of various carbonate minerals into veins accompanied by a release of Ca^{2+} and OH^- enriched water to the surface, creating an environment which promotes rapid precipitation of $CaCO_3$ at surface springs. This environment enables us to apply the recently developed Δ_{47}-Δ_{48} dual clumped isotope analysis to probe kinetic isotope effects (KIEs) and timescales of CO_2 transformation in a region with the potential for geological CO_2 sequestration. We analyzed $CaCO_3$ recovered from various localities and identified significant kinetic fractionations associated with CO_2 absorption in a majority of samples, characterized by enrichment in Δ_{47} values and depletion in Δ_{48} values relative to equilibrium. Surface floes exhibited the largest KIEs ($\Delta\Delta_{47}$: 0.163‰, $\Delta\Delta_{48}$: -0.761‰). Surface floe samples begin to precipitate out of solution within the first hour of CO_2 absorption, and the dissolved inorganic carbon (DIC) pool requires a residence time of >100 hours to achieve isotopic equilibria. The Δ_{48}/Δ_{47} slope of samples from the Cedars (-3.223±0.519; 1 SE) is within the range of published theoretical values designed to constrain CO_2 hydrolysis-related kinetic fractionation (-1.724 to -8.330). The $\Delta_{47}/\delta^{18}O$ slope (-0.009±0.001) and $\Delta_{47}/\delta^{13}C$ slope (0.009±0.001) are roughly consistent with literature values reported from a peridotite in Oman of -0.006±0.002 and -0.005±0.002, respectively. The consistency of slopes in the multi-isotope space suggests the Δ_{47}-Δ_{48} dual carbonate clumped isotope framework can be applied to study CO_2-absorption processes in applied systems, including sites of interest for geological sequestration.

1. Introduction

The rate and mechanism of CO_2 transformation into carbonate minerals in natural alkaline springs and peridotites is of interest because of the potential for permanent, non-toxic CO_2 sequestration. Carbon mineralization at peridotites that host alkaline springs exist worldwide. It is hypothesized that serpentinization, a process that involves the hydration of ultramafic minerals, facilitates the carbon mineralization process in peridotite bodies (Bruni et al., 2002; Falk et al., 2016; García del Real et al., 2016; Kelemen et al., 2017; Suzuki et al., 2017; de Obeso and Kelemen, 2018). Serpentinization can be generally described by reactions 1-3 listed below (Kelemen and Matter, 2008).

$$2Mg_2SiO_4 + Mg_2Si_2O_6 + 4H_2O \rightarrow 2Mg_3Si_2O_5(OH)_4 \tag{1}$$

$$Mg_2SiO_4 + 2CO_2 \rightarrow 2MgCO_3 + SiO_2 \tag{2}$$

$$Mg_2SiO_4 + CaMgSi_2O_6 + 2CO_2 + 2H_2O \rightarrow 2Mg_3Si_2O_5(OH)_4 + CaCO_3 + MgCO_3 \tag{3}$$

Olivine (Mg_2SiO_4) and pyroxene ($Mg_2Si_2O_6$; $CaMgSi_2O_6$) react with CO_2-charged water to form serpentine [$Mg_3Si_2O_5(OH)_4$], magnesite ($MgCO_3$), quartz (SiO_2), calcite ($CaCO_3$), and aragonite ($CaCO_3$). Relatively small amounts of hydromagnesite [$Mg_5(CO_3)_4(OH)_2 \cdot 4H_2O$] (Zedef et al., 2000), brucite [($Mg(OH)_2$] (Moody, 1976), nitromagnesite [$Mg(NO_3)_2$] (Schefer and Grube, 1995), and nesquehonite ($MgCO_3 \cdot 3H_2O$) (Kastrinakis et al., 2021) may also form via reactions 4-7, respectively.

$$5Mg^{2+} + 4CO_3^{2-} + 2OH^- + 4H_2O \rightarrow Mg_5(CO_3)_4(OH)_2 \cdot 4H_2O \tag{4}$$

$$2Mg2SiO_4 + 3H_2O \rightarrow Mg_3Si_2O_5(OH)_4 + Mg(OH)_2 \tag{5}$$

$$2MgO + 4NO_2 + O_2 \rightarrow 2Mg(NO_3)_2 \tag{6}$$

$$Mg^{2+} + CO_2 + 4H_2O \rightarrow MgCO_3 \cdot 2H_2O + 2H^+ \tag{7}$$

Ongoing serpentinization of mantle peridotite bodies by meteoric waters can be identified by highly alkaline water in proximate springs, stable isotope ratios of precipitated carbonate minerals, the formation of travertines, and carbonate veins in the hosting peridotite body (Bruni et al., 2002; Cipolli et al., 2004).

Early research on ultramafic formations undergoing serpentinization led to a conceptual model for this process (Barnes and O'Neil, 1969) (Figure 1). Meteoric groundwater charged with atmospheric CO_2 reacts with the peridotite body near the surface and forms water that is rich in Mg^{2+}-HCO_3^-, termed Type 1 waters (Barnes and O'Neil, 1969). As this water moves underground and encounters the peridotite body, the serpentinization process is catalyzed by CO_2-charged H_2O, leading to the precipitation of $MgCO_3$ and $CaCO_3$ into veins in the peridotite. A sharp elevation in pH accompanies the mineral precipitation due to the enrichment of the water solution with OH^- anions, termed Type 2 water. This Type 2 water also exhibits significant enrichment in Ca^{2+} and depletion in DIC. Type 2 water is brought up to the surface where it interacts with Type 1 water, instantly supersaturating the fluids with respect to carbonate and leading to the precipitation of calcite, aragonite, and travertine in surface springs.

A potential tool for probing carbon mineralization in these settings is carbonate clumped isotope geochemistry. The measurement of carbonate clumped isotopes in minerals precipitated from alkaline fluids can potentially constrain the mechanism(s) of kinetic isotope effects (KIEs) and rate of precipitation (Watkins and Hunt, 2015; Tripati et al., 2015; Guo, 2020; Bajnai et al., 2020). Carbonate clumped isotope analysis measures the relative abundance of multiply (heavy isotope)-substituted CO_2 isotopologues produced from acid digestion of carbonate minerals. When carbonate minerals form at thermodynamic equilibrium, they have a temperature-dependent preference of aggregation based on relative zero-point energies (Ghosh et al., 2006; Schauble et al., 2006). The relative abundance of the most common multiply-substituted mass 47 ($^{13}C^{18}O^{16}O$) and mass 48 ($^{12}C^{18}O^{18}O$) isotopologues are given by equations 8 and 9,

$$\Delta_{47} = (R47_{sample}/R47_{stochastic} - 1) \tag{8}$$

$$\Delta_{48} = (R48_{sample}/R48_{stochastic} - 1) \tag{9}$$

where Ri is the ratio of the minor isotopologues (m/z 47 or m/z 48) relative to the most abundant isotopologue (m/z 44), and $Ri_{stochastic}$ is calculated using the measured abundance of $^{13}C/^{12}C$ and $^{18}O/^{16}O$ (R^{18}) in the sample and the estimated abundance of $^{17}O/^{16}O$ (Eiler, 2007). The latter ratio is estimated from R^{18} assuming a mass-dependent relationship between ^{18}O and ^{17}O (Daëron et al., 2016). The Δ_{47} and Δ_{48} values are given in parts per thousand (‰) (Eiler and Schauble, 2004; Ghosh et al., 2006; Eiler, 2007).

To date, most studies mechanistically exploring KIEs in carbonates using clumped isotopes have focused on isotopic disequilibria in paired Δ_{47} and oxygen isotope ($\delta^{18}O$) signatures. Diffusion has been hypothesized to produce KIEs in Δ_{47}-$\delta^{18}O$ in atmospheric CO_2 and corals (Eiler and Schauble, 2004; Thiagarajan et al., 2011). KIEs in biotic and abiotic systems associated with (de)hydration and (de)hydroxylation reactions can drive deviations from Δ_{47} equilibrium (Ghosh et al., 2006; Guo et al., 2009; Saenger et al., 2012; Falk et al., 2016; Spooner et al., 2016), as can CO_2 degassing, which has been used to explain Δ_{47} disequilibrium in speleothems (Hendy, 1971; Affek et al., 2008; McDermott et al., 2011; Guo and Zhou, 2019). Tang et al. (2014) hypothesized that kinetic fractionation observed in inorganic calcite precipitation experiments at pH ≥ 10 occurred due to the DIC pool not having sufficient time to achieve isotopic equilibrium prior to mineral precipitation and DIC speciation favoring CO_3^{2-} at higher pH.

Previously, Δ_{47} values have been used to study CO_2 absorption-dominant disequilibria processes. One paper reported data from carbonates in hyperalkaline springs at the Oman ophiolite and attributed disequilibria to the increase in CO_2 absorption in water at elevated pH (Falk et al., 2016). This study showed that carbonates from these highly alkaline systems exhibit significant enrichments in Δ_{47}, accompanied by depletion in $\delta^{18}O$ and $\delta^{13}C$. The observed pattern was found to be consistent with CO_2 absorption-driven disequilibrium processes related to the CO_2 hydroxylation reaction being expressed (Falk et al., 2016).

Recent work has shown that the "dual" carbonate clumped isotope system, the paired measurement of Δ_{47} and Δ_{48}, has a characteristic relationship to equilibrium and can be used to study KIEs (Tripati et al., 2015; Fiebig et al., 2019; Guo, 2020; Bajnai et al., 2020; Lucarelli et al., 2023). The equilibrium Δ_{47}-Δ_{48} dual clumped isotope relationship was constrained by theory (Hill et al., 2014; Tripati et al., 2015; Guo, 2020; Hill et al., 2020) and more recently, by measurements from multiple studies(Fiebig et al., 2019, 2021; Bajnai et al., 2020; Lucarelli et al., 2023). However, the use of dual clumped isotope measurements for mechanistic identification of KIEs is

limited. The basis relies on theoretical modeling (Hill et al., 2014; Tripati et al., 2015; Guo, 2020; Hill et al., 2020) that constrain KIEs in Δ_{47}, Δ_{48}, and $\delta^{18}O$ in HCO_3^- and CO_3^{2-} from DIC-H_2O exchange driven disequilibria pathways and (de)hydration and (de)hydroxylation reactions occurring during CO_2 absorption and CO_2 degassing. Applications to identify KIEs has been limited to a small number of measurements from biominerals including warm and cold-water coral, belemnite, and brachiopods, as well as speleothems (Bajnai et al., 2020; Lucarelli et al., 2023).

Here, we apply the novel dual carbonate clumped isotope approach, which combines the measurement of Δ_{47} and Δ_{48}, to minerals from alkaline springs at The Cedars, located in a coastal mountain range formed of peridotite in Northern California. The high alkalinity, elevated pH of 11.5, and low dissolved [CO_2] facilitate the uptake of CO_2 (Lívanský, 1982; Devriendt et al., 2017), which participates in hydration or hydroxylation reactions leading to the formation of HCO_3^- (reactions 10-11). These two reactions are the most important in understanding $^{18}O/^{16}O$ isotopic equilibration as they provide the only route for the direct exchange of O atoms between H_2O and DIC (Zeebe and Wolf-Gladrow, 2001). Reactions 12-14 show the pathway from HCO_3^- to CO_3^{2-} and splitting of water molecules, and reactions 15-16 result in carbonate mineral formation. Reactions 10-16 contribute to isotopic equilibration of DIC in an aqueous solution.

$$CO_2 + H_2O \leftrightarrow H_2CO_3 \leftrightarrow HCO_3^- + H^+ \tag{10}$$

$$CO_2 + OH^- \leftrightarrow HCO_3^- \tag{11}$$

$$HCO_3^- + OH^- \leftrightarrow H_2O + CO_3^{2-} \tag{12}$$

$$HCO_3^- \leftrightarrow H^+ + CO_3^{2-} \tag{13}$$

$$H_2O \leftrightarrow H^+ + OH^- \tag{14}$$

$$Ca^{2+} + HCO_3^- \leftrightarrow CaCO_3 + H^+ \tag{15}$$

$$Ca^{2+} + CO_3^{2-} \leftrightarrow CaCO_3 \tag{16}$$

The amount of time required for clumped and oxygen isotopic equilibrium to be achieved is governed by the temperature-dependent forward and reverse rate constants for the hydration and hydroxylation reactions, as well as DIC speciation (Zeebe and Wolf-Gladrow, 2001). DIC speciation is a function of temperature and pH (Uchikawa and Zeebe, 2012; Tripati et al., 2015). At pH > 10, similar to what is observed in waters in peridotite bodies such as The Cedars, the time to reach equilibration is significantly increased due to DIC speciation being dominated by CO_3^{2-}, resulting in low concentrations of CO_2 remaining for isotopic exchange reactions 10 and 11 (Beck et al., 2005; Tripati et al., 2015; Weise and Kluge, 2020). If the DIC pool does not have sufficient time to achieve isotopic equilibrium before precipitation begins, disequilibrium isotopic compositions may be recorded in the mineral during reactions 15-16.

In this study, we examine the measured departures from equilibrium of dual clumped and bulk ($\delta^{13}C$ and $\delta^{18}O$) isotope values in The Cedars alkaline springs. Our goal is to mechanistically evaluate disequilibria, examine the origin of KIEs in DIC and carbonate minerals, and study the timescales associated with mineral precipitation. Our measurements are combined with modeling

184 to study DIC and mineral isotopic evolution. Finally, we compare our results to published work
185 from other peridotite bodies and evaluate our approach for its potential use in geological CO_2
186 sequestration applications.
187
188 **2. Methods**
189
190 **2.1 The Cedars Samples**
191   The Cedars is part of the Northern California Coastal Mountain Range and is located at
192 N38º37'14.84"/W123º08'02.13 (Figure 2). The Cedars is inside of a 700 km long surrounding
193 body of ultramafic rocks called the Coast Range Ophiolite (CRO). The broader Coastal Mountain
194 Range consists of peridotites in contact with part of the Franciscan Subduction Complex (FSC).
195 The FSC consists of primarily greywacke-type sandstone, greenstone, radiolarian chert, and minor
196 foraminiferal limestone (Blake et al., 2012). The peridotite body has an approximate surface area
197 of 22.4 km^2 (3.5 km width, 6.4 km length) and extends 1-2 km below the surface (Coleman, 2000).
198 The peridotite body consists primarily of olivine, orthopyroxene, and clinopyroxene in varying
199 proportions as harzburgite (75% olivine and 25% orthopyroxene/clinopyroxene) and dunite (100%
200 olivine) (Coleman, 2000). Interactions between the peridotite body and groundwaters derived from
201 multiple sources has resulted in serpentinization of 5-20% of the ultramafic body, particularly
202 around the perimeter that is in contact with the FSC, where the perimeter is predominantly
203 composed of sheared serpentine (Coleman, 2000; Blake et al., 2012).
204   Groundwater discharge from the ultramafic body is highly alkaline, enriched in Ca^{2+} and OH^-
205 , and is brought to the surface through various springs in the area (Coleman, 2004; Sleep et al.,
206 2004) where it mixes with relatively neutral pH surface waters charged with atmospheric CO_2 at
207 an elevation between ~275-335 m above sea level (Barnes and O'Neil, 1969; Morrill et al., 2013).
208   The samples used for this study are comprised of $CaCO_3$ and were collected from The Cedars
209 by Christensen et al. (2021), spanning eight visits in 2013, 2014, 2016, and 2018. Four major sites
210 seen in Figure 2 were sampled: (1) NS1 "Wedding Cake" (samples: A, Q), The Barnes Spring
211 Complex (BSC) (samples: AA, Alpha, C1, P, PA-C2, PB-C2, PE-C2, PE-C3, S, T1, T2, T3a, T3b,
212 T4, T5, U, V, X), Grotto Pool Springs (GPS) (samples: J, K, L), and the "New Pool" (sample: B).
213 The "Wedding Cake" is at the NS1 location above the Mineral Falls. The $CaCO_3$ samples were
214 collected from several different localities adjacent to the springs seen in Figure 2: (1) partially
215 consolidated materials from rims of pools; (2) precipitates from the surface of pools, also known
216 as floes; (3) dendritic forms and encrustations from sites of creek-spring mixing; (4)
217 unconsolidated material, also known as snow, from the bottom of the pools; and (5) solid, old
218 travertine deposits, taken as a hand sample representing different layers, collected from the BSC.
219 Any consolidated, or partially consolidated surface materials were skimmed from the surface or
220 captured on screens based on the location they were collected from. Specific sample information,
221 including composition and location of recovery, is listed in Table 1. The terminology used to
222 describe samples in this paper is after Christensen et al. (2021).
223   Water samples from the high pH springs were taken using a 0.22 µm Millipore filter unit,
224 acidified to a pH of 2 using HNO_3, and collected in high-density polyethylene (HDPE) bottles
225 (Christensen et al., 2021). The pH of the water was measured on site using a Thermo-Scientific,
226 Orion hand-held pH meter. Temperature measurements were taken of the water source at the time
227 of carbonate sample recovery (Christensen et al., 2021).
228
229 **2.2 Analysis and Instrumentation**

All clumped isotopic measurements were made in the Eagle-Tripati laboratory using two Nu Instruments Perspective isotope ratio mass spectrometers (IRMS) with methods described in detail in prior publications (Upadhyay et al., 2021; Lucarelli et al., 2023). Here we will refer to the first IRMS as Nu Perspective-1, and the second as Nu Perspective-2a and Nu Perspective-2b, as measurements on the latter instrument used two configurations. Both instruments and all configurations have been shown to produce statistically indistinguishable Δ_{47} (Upadhyay et al., 2021; Lucarelli et al., 2023) and Δ_{48} values (Lucarelli et al., 2023), with standard values that agree with published values from other laboratories for Δ_{47} (Bernasconi et al., 2021) and Δ_{48} (Bajnai et al., 2020; Fiebig et al., 2021; Swart et al., 2021).

Briefly, we describe analysis and instrumentation here. For this work, measurements were made between September 2018 to November 2021. The general configuration used for clumped isotope measurements on these two instruments is (1) phosphoric acid digestion of 0.5 mg $CaCO_3$, (2) evolved CO_2 gas purification, and (3) isotopic measurements via the mass spectrometer.

The Nu Perspective IRMS is optimized for clumped isotope analysis with secondary electron suppression, which increases the signal-to-noise ratio. Energy filters and quadratic lenses fitted in front of the Faraday collectors for m/z 47, 48, and 49 drives the suppression. The detectors for m/z 44, 45, and 46 are registered through $3x10^8$, $3x10^{10}$, and $3x10^{11}$ Ω resistors, respectively. The detectors for m/z 47, 48, and 49 are registered with $3x10^{12}$ Ω resistors. A dual-inlet system allows for the input of the sample gas and a reference gas controlled by a bellows system that inputs both gasses through a changeover block, so the sample and reference gases can be compared in real-time. The reference gas and sample gas pressure is precisely matched with continuous pressure adjustments to achieve 24 V on mass 44 at the start of every acquisition block, and the pressure varying between 24-9 V during an acquisition block. Data were taken in 3 blocks of 20 cycles, for a total of 60 cycles of sample to standard comparison, with an 8-second changeover delay and 20 seconds of integration per cycle, for a total integration time of 1200 seconds.

Nu Perspective-1 and Nu Perspective-2a used an in-house built, automated system commonly referred to as the "Autoline," similar to the system from Passey et al., (2010). The autoline consists of (1) a Costech Zero Blank autosampler made of stainless steel that is capable of pulling high vacuum, (2) a common acid bath (CAB) containing 105 wt% phosphoric acid where 0.5 mg of $CaCO_3$ is reacted at 90 ℃, (3) cryogenic traps (dry ice and ethanol, and liquid nitrogen) for CO_2 purification through removal of water and other gases with low vapor pressures, and collection of CO_2, (4) an in-line elemental-silver wool (Sigma-Aldrich) column to remove sulfur compounds from the gas mixture, (5) a gas chromatograph (GC) column (UHP Helium carrier gas, Porapak Type-Q TM 50/80 mesh column packing material) held at -20 ℃ during the gas transit to separate CO_2 from the remaining components of the produced gas mixture, and (6) a final cryogenic purification stage before transfer of CO_2 into the bellows of the mass spectrometer.

Nu Perspective-2b uses a Nu Carb Sample Digestion System instead of a CAB, where 0.5 mg of $CaCO_3$ is digested at 70°C in individual glass vials with 105 wt% phosphoric acid. The sample gas is cryogenically purified in liquid nitrogen-cooled tubes called coldfingers before passing through a relatively short GC column packed with Porapak Type-QTM 50/80 and silver wool. This instrument operates under vacuum pressure and does not use a carrier gas.

2.2.1 *Standardization and Data Processing*

Data was processed and corrected using Easotope 64-bit, release version 20201231 (John and Bowen, 2016) with IUPAC parameters (Brand et al., 2010; Daëron et al., 2016). The CO_2 reference gas used to establish real-time comparison to unknown sample compositions was

276 sourced from Oztech and has an isotopic composition as follows: $\delta^{18}O_{VSMOW} = 24.9$ ‰; $\delta^{13}C_{VPDB}$
277 $= -3.56$ ‰. The Δ_{47} values are reported in the Intercarb-Carbon Dioxide Equilibrium Scale (I-
278 CDES) reference frame, meaning they were normalized to nominal carbonate standard values for
279 ETH-1, ETH-2, and ETH-3 determined in Bernasconi et al. (2021), and additional in-house
280 standards with values also determined in the I-CDES reference frame (Upadhyay et al., 2021;
281 Lucarelli et al., 2023). The Δ_{48} values are reported in the Carbon Dioxide Equilibrium Scale (CDES
282 90) reference frame and normalized to carbonate standards values digested at 90 ºC reported in
283 Lucarelli et al. (2023). The standards used in empirical transfer functions (ETFs) for data
284 normalization, using methods detailed in Dennis et al. (2011), include Carmel Chalk, CM Tile
285 (Carrara Marble Tile), ETH-1, ETH-2, ETH-3, ETH-4, and Veinstrom (Upadhyay et al., 2021;
286 Lucarelli et al., 2023). International standards ETH-1 and ETH-2 (Bernasconi et al., 2018, 2021)
287 were used for non-linearity corrections associated with both Δ_{47} versus δ^{47} and Δ_{48} versus δ^{48} raw
288 data. Both the ETFs and nonlinearity corrections are calculated using a moving average of ±10
289 standard replicates. The clumped isotope measurement errors are reported as ±1 standard error
290 (SE) and ±1 standard deviation (SD), and the carbon and oxygen isotope measurement errors are
291 given as ±1 SD. All data regressions were determined in PRISM Version 9.5.0 for macOS using
292 the function "simple linear regression", where the slope and intercept error are reported as ±1 SE.
293 The reproducibility of standard Δ_{47} and Δ_{48} values on each instrument configuration are given in
294 Table S1, and all sample and standard replicate data are reported in Tables S2 and S3,
295 respectively. Figures S1-S3 show the ETH-1 and ETH-2 values from each correction interval.
296 Figure S4 shows the standard residual values (measured value – expected value), and Table S4
297 reports statistical tests (D'Agostino and Pearson test, performed in PRISM) which indicate
298 standard residuals from each instrument configuration were normally distributed. Information on
299 clumped isotope data quality assurance can be found at https://doi.org/10.5281/zenodo.7644586.
300
301 **2.3 Modeling of DIC-H$_2$O-CO$_2$ System Using IsoDIC**
302 To study the evolution of the HCO$_3^-$ and CO$_3^{2-}$ endmembers in a CO$_2$ absorption-driven
303 pathway that simulated the conditions of springs at The Cedars, we used the IsoDIC modeling
304 software developed by Guo and Zhou (2019) and Guo (2020). This modeling software simulates
305 reactions 10-14, predicting kinetic isotope fractionation in oxygen and clumped isotopes in a DIC-
306 H$_2$O-CO$_2$ system from (de)hydration and (de)hydroxylation reactions. The model tracks the
307 isotopologue reactions involving all major isotopes of C and O, for a total of 155 reactions. The
308 forward and reverse rate constants were estimated using equation 17 below,
309
310 $k^* = a_{KIE} * k$ (17)
311
312 where k is the rate constant of the isotopically unsubstituted reactions, and a_{KIE} is the kinetic
313 fractionation factor (KFF) for the isotopically substituted reaction. The product of these variables
314 yields k^*, the modified rate constant for the isotopically substituted reaction. (De)hydration and
315 (de)hydroxylation reactions, reactions 10-11, are the only reactions that contribute to isotopic
316 fractionation where reactions 12-14 are assumed to be at equilibrium due to their relatively fast
317 reaction rates when compared to reactions 10 and 11 (Guo and Zhou, 2019; Guo, 2020).
318 Parameters measured *in-situ* for surface floe samples (Samples L, P, U, V, PE-C2, PB-C2,
319 and X) from The Cedars were used to simulate conditions associated with The Cedars Springs
320 (Morrill et al., 2013). The following parameters were input into the IsoDIC software to perform
321 modeling in the CO$_2$ absorption regime: (1) solution temperature = 17.5 ºC, (2) solution pH = 11.5,

(3) air pCO_2 = 400 ppm, (4) $\delta^{13}C_{VPDB}$ of air = -8.431 ‰, and (5) $\delta^{18}O_{VPDB}$ of water = -36.3±0.6‰, taken as the average of measurements from the NS1, GSP1, and BSC locations (Morrill et al., 2013). The system evolution time parameter was set to 1, 10, 50, 100, and 1000 hours to simulate different timescales for the evolution of the HCO_3^- and CO_3^{2-} DIC species. We note that modern samples are collected from locations where surface creek (pH = 8.7) and spring waters (pH = 11.5) are mixing, resulting in a potential drop in pH to an intermediate value (pH = 8.7 to 11.5) that would reduce equilibration times from the longer values associated with highly alkaline solutions. The equations used by this model are described in the Supplementary Material-1.

The conversion of carbonate minerals into gaseous CO_2 is associated with a temperature-dependent preferential removal of O^{16} relative to O^{18} and is corrected by an acid fractionation factor (AFF), denoted by y in equations 18 and 19 (Guo et al., 2009).

$$\Delta_{47} = \Delta_{63} + y \tag{18}$$

$$\Delta_{48} = \Delta_{64} + y \tag{19}$$

An AFF is applied to measured Δ_{47} and Δ_{48} values for comparison to modeled Δ_{63} and Δ_{64} values. The reference frame and temperature to which the value is being converted also dictates the value of y. An AFF of y = 0.196 ‰ was used in the conversion between Δ_{63} and Δ_{47} values, and an AFF of y = 0.131 ‰ was used in the conversion between Δ_{64} and Δ_{48} values (Lucarelli et al., 2023).

2.4 Modeling of the CaCO₃-DIC-H₂O System Using COAD

To model the KIEs in the clumped and stable isotope data of the carbonate minerals with respect to the conditions at The Cedars, we used the COAD (Carbon, Oxygen, α, Δ) model (Watkins and Devriendt, 2021), adapted from the ExClump38 model (Chen et al., 2018; Uchikawa et al., 2021). The COAD model uses two MATLAB scripts to simulate KIEs associated with exchange reactions in the DIC-H₂O system and crystal growth reactions in the CaCO₃-DIC system (Watkins and Devriendt, 2021). We used this model in addition to the IsoDIC model because it takes mineral growth rate into account, which has been hypothesized to influence the clumped isotope composition (Watkins and Hunt, 2015; Tripati et al., 2015). The model was first developed by Chen et al. (2018) for calculations associated with C and O isotopes, and then expanded by Uchikawa et al. (2021) to include Δ_{47} and labeled ExClump38. It was further expanded to include calculation of Δ_{48} values by Watkins and Devriendt (2021).

The COAD model used the same KFFs (Guo, 2020) and input parameters for isotopic values, temperature, and pH as the IsoDIC model (see the previous section). The COAD model uses a total of 17 differential equations to model reactions 10-16, which track the evolution of the $\delta^{18}O$, $\delta^{13}C$, Δ_{47}, and Δ_{48} values of DIC species in solution and the precipitating CaCO₃ (Watkins and Hunt, 2015; Watkins and Devriendt, 2021). The rate constants associated with precipitation reactions 15 and 16 are mass-dependent, and the flux of precipitated CaCO₃ is controlled by the $[Ca^{2+}]$ and $[CO_3^{2-}]$ (Watkins and Hunt, 2015). In contrast to the IsoDIC model, this model only describes the most abundant isotopologues for the respective masses, while IsoDIC describes all isotopologues in the DIC-H₂O system. The COAD model was also used to calculate the evolution in isotopic values from varying mineral precipitation rate (R_p). A description of the equations and parameters used are reported in Supplemental Material-1. The code used is available at https://doi.org/10.5281/zenodo.7644586.

2.5 Estimation of CO₂ Sequestered at The Cedars

Due to the similarity in rock composition and water pH in the Samail Oman and The Cedars peridotite and associated springs (Kelemen and Matter, 2008; Morrill et al., 2013; Christensen et al., 2021), we estimated the rate and amount of CO_2 that could naturally be sequestered at The Cedars based on an approach used in previous work from Kelemen and Matter (2008) for a peridotite body in Oman. Kelemen and Matter (2008) estimated that in the Omani ophiolite, the travertines and carbonate veins comprised a volume of roughly $5.5 \times 10^7 \, m^3$, or a minimum of $\approx 10^{11} \, kg$ of CO_2. In addition, for the determination of rates of carbonation for the two different types of waters (Figure 1), they make two key assumptions. First, in Type 1 waters, they assume the complete consumption of DIC to precipitate carbonate minerals as Type 2 waters are formed. Second, they assume that differences in dissolved Ca between the two types of waters leads to calcite precipitation as Type 2 waters reach the surface. Using this approach, they calculate that carbonate mineralization in the region consumes ~$4 \times 10^7 \, kg$ of atmospheric CO_2 per year, or ≈ 2 tons/km³/year of peridotite.

We also estimated the total sequestration potential at The Cedars. For this calculation, we summed the amount of CO_2 that would be consumed if the total amount of Mg, Ca, and Fe in relict olivine was consumed by carbonation. We assumed that The Cedars peridotite is composed of 70 % olivine (Blake et al., 2012; Morrill et al., 2013), has a volume of 44.8 km³ (Coleman, 2000), a density of partially serpentinized peridotite of 2800 km/m³ (Carnevale, 2013), total mass of $1.25 \times 10^{14} \, kg$ (calculated from the volume and density), and a carbonation rate of 1 % (Kelemen and Matter, 2008). Below, we show how this calculation was performed for Mg.

$$(1.25 \times 10^{14} \, kg) \times 0.70 \times 0.4382 \times 0.01 \times \frac{CO_2 \; 44 \text{ g/mol}}{Mg \; 24.3 \text{ g/mol}} = 7.0 \times 10^{11} \, kg \; CO_2 \text{ sequestered}$$

We used the conservative estimate of calcite growth rate in The Cedars springs of 4.8×10^7 mol/m²/s (Christensen et al., 2021) to estimate the rate of CO_2 sequestered in the springs per year. For comparison, we report a set of calculations for the CRO from Carnevale (2013) that also utilize the methods of Kelemen and Matter (2008). To estimate the amount of CO_2 sequestered in the CRO per year, we used the CO_2 sequestration potential reported in Carnavale (2013) and the natural carbonation rate for peridotite determined in Kelemen and Matter (2008).

Additionally, Kelemen and Matter (2008) assumed the natural rates of CO_2 uptake could be enhanced by ~10^6 times by drilling and hydraulic fracturing of the rock to increase the reactive surface area, initial heating of the rock to 185 °C using hot fluids, followed by the injection of CO_2 (pressure = 300 bars, temperature = 25 °C, flow rate = 0.040 m/s) (Kelemen and Matter, 2008). They estimate this would result in a sequestration rate of ~2×10^9 tons of CO_2 sequestered per km³. This rate was used to estimate the time elapsed before all peridotite would be converted into carbonate minerals from enhanced in situ carbonation at The Cedars, CRO, and Oman ophiolite. The parameters used in all calculations are reported in Table S5.

3. Results

3.1 Dual Clumped Isotope Analysis

Dual clumped isotope values (Δ_{47}, Δ_{48}) are reported for samples from The Cedars in Figure 3 and Table 2. The Δ_{47} and Δ_{48} values range from 0.595‰ to 0.791‰ and -0.506‰ to 0.282‰,

respectively. The samples that are within error (±1 SE) of an equilibrium regression (Lucarelli et al., 2023) are A, AA, B, and J. All other samples exhibit apparent KIEs, with the greatest departure from equilibrium in sample V (Δ_{47} = 0.779‰; Δ_{48} = -0.506‰ (Figure 3). The sampling location of each sample can be seen in Figure 1. A linear regression of the Δ_{48}-Δ_{47} values from The Cedars yields a slope of -3.223±0.519.

3.2 Clumped and Stable Isotopes

The δ^{18}O and δ^{13}C values for The Cedars calcites range from -19.3‰ to -0.1‰ and -27.3‰ to -9.2‰, respectively (Table 2). The Δ_{47} of modern and Holocene calcite samples from The Cedars are plotted versus δ^{18}O and δ^{13}C and compared to calcite samples from alkaline springs in the Oman ophiolite (Falk et al., 2016) (Figure 4A, C). The measured values from The Cedars and Oman are also compared to calculated equilibrium values. The calculated equilibrium $\delta^{18}O_{CaCO3}$ range was determined to be -8.2‰ to -6.6‰ for calcite and aragonite (Kim and O'Neil, 1997; Kim et al., 2007; Dietzel et al., 2009), given The Cedars $\delta^{18}O_{water}$ value of -36.3±0.6‰, taken as the average of measurements from the NS1, GSP1, and BSC locations (Morrill et al., 2013). The equilibrium Δ_{47} value (Lucarelli et al., 2023) for the average water temperature of 17.5±1 °C (Christensen et al., 2021; Morrill et al., 2013) was determined to be 0.616±0.003‰. All samples show departures from equilibrium oxygen isotope values.

Linear regressions through The Cedars and Oman datasets are in strong agreement. The Δ_{47}/δ^{18}O and Δ_{47}/δ^{13}C data regressions for The Cedars samples both exhibit slopes of -0.009±0.001 (Figure 4A, C). The Δ_{47}/δ^{18}O and Δ_{47}/δ^{13}C data regressions for the Oman samples (Falk et al., 2016) exhibit slopes of -0.006±0.002 and -0.005±0.002, respectively. When The Cedars and Oman datasets are combined, the slopes of the Δ_{47}/δ^{18}O and Δ_{47}/δ^{13}C data regressions are -0.007±0.001 and -0.006±0.001, respectively.

The Δ_{48} versus δ^{18}O and δ^{13}C values for The Cedars are also reported (Figure 4B, D; Table 2), and compared to equilibrium. The equilibrium Δ_{48} value (Lucarelli et al., 2023) for the average water temperature of 17.5±1 °C (Morrill et al., 2013; Christensen et al., 2021) was determined to be 0.255±0.00‰. The Δ_{48}/δ^{18}O and Δ_{48}/δ^{13}C regression slopes are 0.041±0.003 and 0.038±0.005, respectively.

3.3 Clumped and Oxygen Isotope Disequilibrium

The extent of clumped and oxygen isotope disequilibrium ($\Delta\Delta_{47}$, $\Delta\Delta_{48}$, and $\Delta\delta^{18}$O) in The Cedars was calculated by taking the difference between the measured values and calculated equilibrium values (Kim and O'Neil, 1997; Kim et al., 2007; Dietzel et al., 2009; Lucarelli et al., 2023) (Table 2). The $\Delta\Delta_{47}$, $\Delta\Delta_{48}$, and $\Delta\delta^{18}$O values are compared to theoretical slopes determined by Guo (2020) for various kinetic processes (Figure 5). The $\Delta\delta^{18}$O values range from -12.7‰ to 7.2‰, while $\Delta\Delta_{47}$ and $\Delta\Delta_{48}$ values range from -0.021‰ to 0.175‰ and -0.761‰ to 0.027‰, respectively. The slopes of the $\Delta\Delta_{47}$/$\Delta\delta^{18}$O, $\Delta\Delta_{48}$/$\Delta\delta^{18}$O, and $\Delta\Delta_{48}$/$\Delta\Delta_{47}$ are -0.009±0.001, 0.040±0.003, and -3.223±0.519, respectively.

3.4 Modeled Clumped Isotope Evolution

Measured Δ_{47} and Δ_{48} values for The Cedars samples were compared to IsoDIC (Guo, 2020) model predictions for the time-dependent isotopic evolution of HCO_3^- and CO_3^{2-} (Figure 6A). The measured values are consistent with the range of Δ_{47} and Δ_{48} values predicted by the model for HCO_3^- and CO_3^{2-}. The measured Δ_{47} and Δ_{48} values were also compared to model predictions for $CaCO_3$, HCO_3^-, CO_3^{2-}, and equilibrated inorganic carbon (EIC) using the COAD model (Watkins

and Devriendt, 2021) (Figure 6B-D). Measured $\delta^{18}O$ and Δ_{47} values are largely consistent with model predicted values, however, the Δ_{48} values for the ancient travertine samples and snow samples collected from the bottom of the pool (Table 1) were offset from the COAD model predicted values for $CaCO_3$ by up to 0.1 ‰ (Figure 6D).

The average Δ_{47} and Δ_{48} values and growth rate for samples with relatively large KIEs that were collected at the BSC springs location (samples U, V, X; Figure 2) were compared to COAD model predictions for the evolution of clumped isotope values of calcite from varying precipitation rate (Figure 6E-F). The model accurately predicted the measured Δ_{47} value of 0.744±0.010‰ within 1 SE, while the measured Δ_{48} value of -0.407±0.037‰ was offset from the model predicted value of -0.264‰ by 0.143‰.

3.5 CO₂ Sequestration

We estimate the peridotite body at The Cedars could sequester a maximum of $\sim7.39 \times 10^8$ tons of CO_2 at a natural rate of ~63 tons/year. It would take $\sim1 \times 10^7$ years to reach the maximum amount of sequestration (Figure 7). The Cedars springs could sequester an additional ~4 tons/year. If we utilize estimates of the volume and total sequestration potential of the CRO (Carnevale, 2013), we estimate that $\sim1.2 \times 10^4$ tons of CO_2 could be naturally sequestered per year at the CRO, with the maximum CO_2 sequestration potential achieved after $\sim8.3 \times 10^6$ years. If the enhanced *in situ* carbonation rate of $\sim2 \times 10^9$ tons $CO_2/km^3/year$ described in Kelemen and Matter (2008) were used, all olivine in the CRO could be converted into carbonate minerals in less than 1 year.

4. Discussion

4.1 Broad Patterns in Multi-Isotope Space: Comparison of Sample Sets

The similarity in $\Delta_{47}/\delta^{18}O$ and $\Delta_{47}/\delta^{13}C$ regression slopes for The Cedars data and data from surface springs and veins in the Samail ophiolite of Oman (Falk et al., 2016) (Figure 4A, C) suggest the same processes are driving disequilibrium in both systems. However, regional, and possible local and temporal, variations in the $\delta^{18}O$ of waters, and $\delta^{13}C$ of DIC, also are reflected in these data. For example, the Oman dataset (Falk et al., 2016) may have larger fluctuations in $\delta^{13}C$ and $\delta^{18}O$ due to the amount and type of samples analyzed, and greater fluctuations in DIC $\delta^{13}C$ and meteoric water $\delta^{18}O$ due to the significantly larger area, 200 km x 50 km, of the Oman site (Christensen et al., 2021). In contrast, the Δ_{47}-Δ_{48} dual clumped isotope approach allows for mechanistic fingerprinting of the processes associated with disequilibria, and a rough estimation of timescales for equilibration. This represents a major advancement in the clumped isotope field as data from different localities, natural and synthetic, can be directly compared for potential sources of disequilibrium. An additional benefit of clumped isotopes is the method can be used without knowledge of additional parameters such as the isotopic composition of the parent fluid or DIC source.

The majority of Cedars samples exhibit an enrichment in Δ_{47} accompanied by a depletion in Δ_{48}, with a $\Delta\Delta_{48}/\Delta\Delta_{47}$ slope of -3.223±0.519. Our observed slope is intermediate between the theoretically calculated slopes for KIEs from CO_2 hydration and hydroxylation reactions during CO_2 absorption (25 °C; pH 9) and in high pH travertine (28 °C; pH 11.5), which have slopes of -1.72 and -8.33, respectively (Guo, 2020) (Figure 5). Thus, the disequilibria at The Cedars and Oman are occurring through a similar pathway that is largely associated with CO_2 hydroxylation. We note a similar trend was also reported by Bajnai et al. (2020) in their dual-clumped investigation of cold-water coral, warm-water coral, and brachiopods, and in a cold-water coral

sample reported by Lucarelli et al. (2023). Both studies concluded hydration/hydroxylation during CO_2 absorption drove kinetic biases in the dual clumped isotope values.

4.2 (Dis)Equilibrium Within The Cedars Depends on Sample Location

Sample location within The Cedars was a major factor influencing whether bulk and clumped isotopic data exhibited departures from equilibria, likely linked to variations in DIC sources (i.e., Type 1 and Type 2 waters) and equilibration time. Modern samples L, P, U, V, PB-C2, and PE-C2 collected from surface pool floes located at the BSC and GPS locations (Figure 2) exhibited the greatest KIEs (Figures 3-6). At these two localities, KIEs could be related to the rapid uptake of CO_2 at the surface, leading to similarly rapid carbonate mineral precipitation at the air and water interface. These results would be consistent with the interpretations of bulk stable isotopic data by Christensen et al. (2021), who investigated the dynamics associated with $CaCO_3$ precipitation and stable isotope fractionation in surface floes, and argued that at The Cedars, KIEs may be the largest when $CaCO_3$ precipitates at the surface of the springs. The BSC location had a high saturation state (Ω) value of ~13, while the GPS location had an Ω value of ~5. The $[CO_2]$ at the surface layer at the BSC location was calculated to be 1.6×10^{-5} mol/kg-solution, several orders of magnitude higher than the concentration of the bulk pool. The rate of Ca^{2+} replenishment from the springs at the BSC was determined to be 1.5×10^{-6} mol/s, which is comparable to the DIC flux from the atmosphere. The CO_2 from the atmosphere is converted to HCO_3^- via hydroxylation (reaction 11), with rapid and near-quantitative conversion to CO_3^{2-} (Tripati et al., 2015). With this higher influx of CO_2 and precipitation of $CaCO_3$, the surface pH is reduced slightly from 11.5 in the bulk pool springs to 11.0 at the surface (Christensen et al., 2021). However, the pH is still high enough to favor CO_3^{2-} DIC speciation (Uchikawa and Zeebe, 2012; Tripati et al., 2015) preventing isotopic equilibrium through exchange reactions associated with the other DIC species. In addition, because the concentration of DIC is so high at the surface due to the large CO_2 gradient between the water and atmosphere, the supersaturation state of $CaCO_3$ is also considerably high, further promoting rapid precipitation of $CaCO_3$ outside of isotopic equilibrium (Christensen et al., 2021).

The modern "snow" samples C1, K, PA-C2, PE-C3 and PB-C1 exhibited KIEs that were intermediate between equilibrium and pool floe samples (Figure 3). The term snow is used to describe the physical appearance of fine particulates of $CaCO_3$ aggregating at the bottom of the pools, however, their texture is similar to surface floe samples (Christensen et al., 2021). The thin-film model (Christensen et al., 2021) for surface dynamics suggests that as the surface floes thicken or are perturbed by falling debris, $CaCO_3$ aggregates detach and sink deeper into the springs. The floes would carry some surface waters with the particles (Christensen et al., 2021), and thus could mix in a pool of DIC that is not in isotopic equilibrium, driving KIEs in the clumped and bulk isotope signatures. Even though these detached layers, composed of a mixture of particle aggregates and solution, have moved away from the surface where the majority of rapid precipitation is occurring, isotopic equilibration of DIC within the detached layer is still hindered by the high pH of 11.5 (Beck et al., 2005), which favors hydroxylation and CO_3^{2-} as the most abundant DIC species (Tripati et al., 2015). Given water temperatures, DIC in this fragmented layer can retain its kinetic signature for tens of days at a pH of 11.5 (Usdowski et al., 1991; Beck et al., 2005) which can contribute to the KIEs in dual clumped and bulk isotopes. DIC mixing can also drive deviations from equilibrium in Δ_{47} values (Defliese and Lohmann, 2015).

Modern samples A, AA, B, and J fell within 1 SE of clumped isotope equilibrium (Figure 3). They were collected where fresh creek water mixed with spring water at the New Pool and BSC localities, where the pH and the influx of Ca^{2+} are reduced, leading to potentially more

552 favorable conditions for isotopic equilibration in the DIC-H_2O-CO_2 system. These samples reflect
553 the composition of isotopically equilibrated DIC from the creek or surface water (pH 7.8-8.7) that
554 occasionally mixes with the high-pH springs (Christensen et al., 2021). The Δ_{47}-reconstructed
555 temperature considering the near equilibrium samples is 13.9±3.8 °C and 14.2±3.5 °C, using
556 calibrations from Lucarelli et al. (2023) and Andersen et al. (2021), respectively. These
557 reconstructed temperatures are within error (1 SD) of the average yearly temperature at The Cedars
558 of 17.5±1 °C (Morrill et al., 2013; Christensen et al., 2021).
559   Ancient travertine samples collected from rim formations at the NS1 locality (Alpha, T1,
560 T2, T3a, T3b, T4, and T5) display a range of disequilibrium values (Figures 3-6). This range could
561 be due to post-depositional events such as recrystallization in the presence of surface and
562 groundwater mixing, which could have shifted disequilibrium isotopic values towards equilibrium
563 in samples T1, T4, and T5. This would be analogous to what Falk et al. (2016) hypothesized
564 occurred in Oman, where the absence of aragonite in travertine samples may have indicated post-
565 depositional events had taken place, thereby influencing isotopic values.
566
4.3 Overall Conditions at The Cedars Result in Isotopic Disequilibrium

568   Several factors control the expression of KIEs in carbonate minerals from The Cedars.
569 These include the hydroxylation favored pathway, DIC speciation, increased rate of CO_2 uptake
570 into the system, and mineral precipitation prior to isotopic equilibria. Because Type 1 and 2 waters
571 are readily mixing at the surface, a hyperalkaline environment (pH > 11) is created due to excess
572 OH^- anions present in Type 2 fluids. At a pH > 10, the hydroxylation pathway represents >95%
573 of reactions transforming CO_2 to HCO_3^- (McConnaughey, 1989). This high pH also creates an
574 environment that facilitates rapid uptake of CO_2 into the aqueous media (Lerman and Stumm,
575 1989) due to the concentration gradient created by the DIC speciation preference of CO_3^{2-} at pH >
576 10 (Hill et al., 2014; Tripati et al., 2015). This condition, coupled with the rapid precipitation of
577 $CaCO_3$ due to the high saturation state (Christensen et al., 2021), creates an even stronger gradient,
578 further increasing the uptake of CO_2 from the atmosphere. The forward reaction rate associated
579 with CO_2 hydroxylation is >1000 times the reverse reaction (Christensen et al., 2021), creating a
580 pathway that is approximately unidirectional. We hypothesize this is preventing backwards
581 conversion which is essential for O isotope exchange that would facilitate $\delta^{18}O$, Δ_{47}, and Δ_{48}
582 equilibrium. The high pH results in a much greater equilibration time (>40 days) being required
583 for the DIC pool to achieve clumped and oxygen isotopic equilibria prior to mineral precipitation
584 (Beck et al., 2005; Tripati et al., 2015; Guo, 2020; Uchikawa et al., 2021). As the system moves
585 into the deeper parts of the spring pool (below 100 µm), there are additional fluxes including
586 advection and diffusion of Type 2 waters, $CaCO_3$ precipitation, and EIC contribution from the
587 surface.
588
4.4 Examination of Kinetic Isotope Effects Using Modeling

590   IsoDIC (Guo, 2020) modeling of disequilibria in the DIC pool used input parameters taken
591 from the surface floe conditions of The Cedars and accurately predicted the measured range of Δ_{47}
592 and Δ_{48} values (Figure 6A). The model was used to predict the evolution of disequilibria associated
593 with HCO_3^- and CO_3^{2-} with respect to residence time in the system. The model indicated a rapid
594 departure away from equilibria with maximum disequilibria achieved at ~1 hour of DIC residence
595 time. This initial departure rebounds back to equilibrium as the system has more time equilibrate,
596 where equilibrium is eventually achieved after ~1000 hours. Due to the low [CO_2] from DIC
597 speciation favoring CO_3^{2-} at high pH (Beck et al., 2005; Tripati et al., 2015), the migration back to

598 equilibria at these conditions is very slow. The IsoDIC (Guo, 2020) model can be used to predict
599 the approximate timeframe associated with precipitation at the surface, which we hypothesize to
600 be ≤1 hour from when CO_2 is introduced into the surface spring system (Figure 6A). A caveat is
601 that this model only considers the KIEs associated with the DIC pool and does not factor those
602 associated with mineral precipitation.
603   Since the IsoDIC model did not consider KIEs associated with mineral precipitation,
604 isotopic evolution was also predicted with the COAD model (Watkins and Devriendt, 2021), which
605 does predict KIEs from precipitation, using the same input parameters as for the IsoDIC model.
606 This model predicted a similar trend for Δ_{47} and Δ_{48} (Figure 6B) when compared to the IsoDIC
607 model, in terms of migration from equilibrium to disequilibrium. However, while the models
608 starting values for CO_3^{2-} and HCO_3^- are very similar, as modeled precipitation starts in the COAD
609 model, the associated KIEs from precipitation result in a maximum difference of ~0.10‰ between
610 the simulated CO_3^{2-} and HCO_3^- values from the two models. Additionally, the measured Δ_{47} values
611 and COAD predictions are in good agreement (Figure 6C), while some measured Δ_{48} values for
612 travertine samples and snow samples collected from the bottom of the pool (Table 1) deviate from
613 model predicted Δ_{48} values by up to 0.1 ‰ (Figure 6D). The ancient travertine samples (T1, T2,
614 T3a, T3b, T4, T5) contained multiple layers, and therefore mixing may impact clumped isotopes
615 (Eiler and Schauble, 2004; Defliese and Lohmann, 2015), and there is no current knowledge of
616 possible differences in travertine versus typical calcite Δ_{48} values. Mixing may also bias clumped
617 isotope values in the snow samples, which may experience temporal variations in DIC isotopic
618 composition. Further, some of the snow samples have mixed minerology (aragonite, calcite,
619 brucite), such as samples PB-C1, PE-C2, and PE-C2 (Table 1). The brucite [Mg(OH)$_2$]
620 composition ranges from 4-7 %, which has unknown effects on acid digestion and potentially the
621 clumped isotope values.
622   COAD (Watkins and Devriendt, 2021) modeling enables us to determine and predict the
623 rates of mineral precipitation associated with the respective system, which is constrained by
624 measured dual clumped isotope values. The COAD model was also used to predict the dependence
625 of Δ_{47} and Δ_{48} values from The Cedars samples on the precipitation rate (Figure 6E-F). The model
626 accurately predicted the average Δ_{47} value at the BSC springs, given the measured precipitation
627 rate (Christensen et al., 2021). Comparison of dual clumped data to model results supports a natural
628 rate of carbonate precipitation of ~4.8 × 10^{-7} mol/m^2/s (Figure 6E). However, the model
629 underpredicted the average Δ_{48} value (Figure 6F). This may be due to greater measurement
630 uncertainty for Δ_{48}, which is an order of magnitude greater than for Δ_{47} (1 SE for Δ_{47} ≈ 0.001; 1
631 SE for Δ_{48} ≈ 0.01), and no previous experimental constraints on how Δ_{48} values change from
632 increased precipitation rates.
633   We find the two models provide a slightly different set of tools. The IsoDIC model provides
634 greater insights into the timescales associated with achieving (dis)equilibrium within a DIC pool,
635 while the COAD model may more accurately predict mineral isotopic compositions and for when
636 mineral growth is moderately rapid. For the IsoDIC model, accurately measured Δ_{47} and Δ_{48} values
637 can be compared to model predictions, which depend on DIC residence time, to predict the elapsed
638 time before the start of mineral growth. For the COAD model, accurately measured Δ_{47} values
639 (and possibly Δ_{48} values) can be compared to model predicted values which depend on
640 precipitation rate to predict mineral precipitation rate.
641   Field measurements and modeling may be useful for application to other peridotite bodies
642 to help determine the natural mineral precipitation rates and DIC residence time. Our work here
643 shows this approach is useful for predicting the natural rates of CO_2 uptake. If the rate of CO_2

644 uptake was enhanced using a feed of high-pressure CO_2 and hydraulic fracturing, dual clumped
645 isotope measurements could be interpreted within a modeling framework to evaluate the enhanced
646 rates of DIC equilibration and mineral formation.
647
648 **4.5 Potential CO_2 Sequestration Application**
649   Assuming the natural carbonation rate of peridotite consumes ~2 tons of CO_2/km^3/year
650 (Kelemen and Matter, 2008), then the peridotite at The Cedars, surrounding ophiolite in the Coast
651 Range, and ophiolite in Oman consume ~90, ~1.1×10^4, and ~4.2×10^4 tons of CO_2 per year,
652 respectively (Figure 7). At the natural rate, the peridotite at The Cedars would take >10^6 years to
653 achieve the maximum CO_2 sequestration potential of ~7.4×10^8 tons. The peridotite at the CRO
654 and Oman would take >10^6 and >10^9 years to reach their CO_2 sequestrations potentials of ~$9.7 \times$
655 10^{10} (Carnavale, 2013) and ~7.7×10^{13} (Kelemen and Matter, 2008) tons, respectively. While
656 these ultramafic formations provide an important natural CO_2 sink, the total yearly sequestration
657 represents <<1% of current global CO_2 emissions of 34.9×10^9 tons (Liu et al., 2022).
658   Previous work by Kelemen and Matter (2008) proposed a method for enhanced *in situ*
659 carbonation of peridotite for the Samail Ophiolite in Oman. This method greatly enhances the
660 natural carbonation reaction (reaction 10) rate by up to 1×10^6 times by drilling and hydraulic
661 fracturing of the rock to increase the reactive surface area, initial heating of the rock to 185 °C
662 using hot fluids, followed by the injection of CO_2 (pressure = 300 bars, temperature = 25 °C, flow
663 rate = 0.040 m/s) (Kelemen and Matter, 2008). After the initial heating, the exothermic carbonation
664 reaction maintains the system temperature at 185 °C (Kelemen and Matter, 2008). As the reactive
665 surface becomes depleted, the rock may require additional fracturing, although some cracking may
666 occur from the temperature changes and increases in solid volume from mineral hydration and
667 carbonation (Kelemen and Matter, 2008). If we assume the fully catalyzed reaction rate of ~$2 \times$
668 10^9 tons of CO_2 sequestered per year, all Mg, Ca, and Fe in the CRO and Oman peridotite could
669 be converted into carbonate minerals in less than 2 years (Figure 7). This would consume an
670 enormous amount of CO_2, totaling ~7.7×10^{13} tons, which is equivalent to >2000 years of CO_2
671 emissions if we were to continue emitting the same amount as we are at present.
672   A hurdle to employing mineral carbonation technology in peridotite formations is that ~1
673 million drill holes (Kelemen et al., 2011) may be required to offset 34.9×10^9 tons (Liu et al.,
674 2022) of anthropogenic CO_2 emissions per year. Further, these operations could result in
675 deforestation (Drohan and Brittingham, 2012), loss of animal habitats (Kiviat, 2013), and
676 contaminated wells (Holzman, 2011), as has been observed with fracking. However, it is notable
677 that the in-situ CO_2 sequestration potential in peridotite bodies is high when compared to other
678 potential technologies. High-temperature mineral carbonation reactors, which would use mineral
679 feedstock from mines and direct CO_2 injection, could rapidly convert serpentine and olivine to
680 magnesite and quartz, resulting in ~8.8×10^5 to ~8.8×10^6 tons of CO_2 sequestered per year
681 (Power et al., 2013). The injection of CO_2 into ponds containing serpentinite mine tailings could
682 sequester up to ~1×10^6 tons of CO_2 per year (Power et al., 2013). This may be enhanced if the
683 ponds utilize photoautotrophic microbes, such as algae and cyanobacteria, which use CO_2 as an
684 energy source (Power et al., 2011). It is likely that multiple strategies will need to be used in
685 parallel to reach global carbon dioxide reduction goals, which are 10 Gt/yr by 2050 and 20 Gt/yr
686 by 2100 (UNEP, 2019).
687
688 **5. Conclusions**
689

690   We analyzed carbonate mineral samples collected from springs at The Cedars, a peridotite
691   body in Northern California, for dual clumped isotopes. We combined measured Δ_{47}, Δ_{48}, $\delta^{18}O$,
692   and $\delta^{13}C$ and model calculations to study kinetic isotope effects associated with CO_2 absorption
693   and transformation of DIC. Our work suggests kinetic biases in dual clumped and bulk isotope
694   values arise due to carbonate mineral precipitation from highly alkaline waters through a CO_2
695   absorption-driven pathway. Our analysis indicates that the largest KIEs are from samples
696   recovered from surface floes where there is sufficient contact with the spring waters and the
697   atmosphere where CO_2 absorption and rapid precipitation conditions are favored. Modern samples
698   with isotopic values within error of equilibrium occur in locations where there is significant mixing
699   of surface and spring waters. Other samples with kinetically biased isotopic values include "snow"
700   samples recovered from the bottom of springs and ancient travertine samples. We report slopes
701   (Δ_{48}/Δ_{47}, $\Delta_{47}/\delta^{18}O$, $\Delta_{48}/\delta^{18}O$, $\Delta_{47}/\delta^{13}C$, $\Delta_{48}/\delta^{13}C$) for CO_2 (de)hydration and (de)hydroxylation
702   disequilibria processes from The Cedars samples. The slopes are consistent with $\Delta_{47}/\delta^{18}O$ and
703   $\Delta_{47}/\delta^{13}C$ slopes from a peridotite body in Oman, as well modeling predictions for KIEs from CO_2
704   (de)hydration and (de)hydroxylation.
705   This work sets up the potential use of the Δ_{47}-Δ_{48} dual clumped isotope method, combined
706   with modeling, to examine potential sites of interest for geological CO_2 sequestration, including
707   in the Coast Ranges and other peridotite bodies. This relatively non-invasive method can be used
708   to determine the natural rate of CO_2 uptake, mineral precipitation rate, and for determining
709   evolution time and (dis)equilibria in DIC. We recommend expansion of dual clumped isotope
710   research into carbonate minerals precipitating from peridotite veins to compare surface and
711   subsurface processes, and better understand the feasibility of sites for CO_2 sequestration.
712
713   **Declaration of Competing Interests**
714   The authors declare that they have no known competing financial interests or personal
715   relationships that could have appeared to influence the work reported in this paper.
716

733

734   **Author Contributions**

Appendix A. Supplementary material

Supplementary Material-1 contains equations and parameters used for modeling. Supplementary Material-2 contains figures demonstrating instrument performance and standard values used in data corrections. Supplementary Material-3 contains raw data for samples and standards, statistical analyses of standards, and parameters used in CO_2 sequestration calculations.
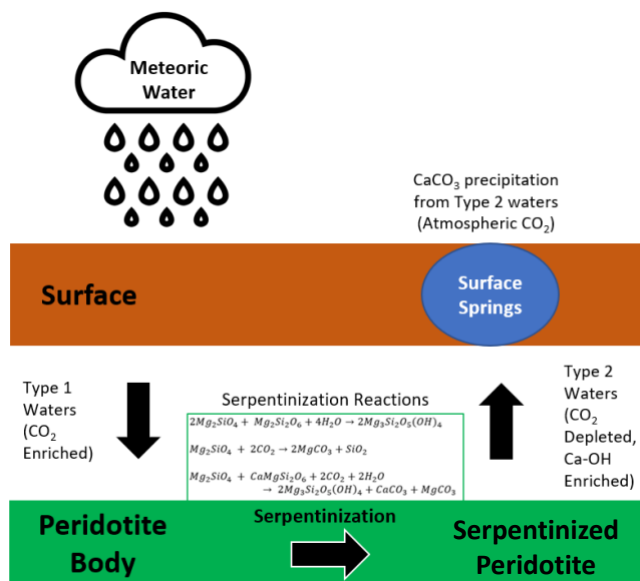
Figures

Figure 1. Processes associated with CO_2 absorption and transformation at The Cedars. Surface waters from meteoric sources are enriched with CO_2 from the atmosphere ("Type 1" waters) and then seep into the ground and interact with ultramafic peridotite. Through a series of serpentinization reactions (reactions 1-3), various carbonate minerals precipitate and are sequestered in pores and fractures resulting in veins in the peridotite body. Reaction by-products are ejected into pore waters, creating waters which are enriched in Ca^{2+} and OH^- ions, and depleted in CO_2 ("Type 2" waters), which are then shuttled to the surface. Type 1 and Type 2 waters interact at the surface in the presence of atmospheric CO_2, resulting in rapid precipitation of $CaCO_3$. Terminology from Barnes and O'Neil (1969).
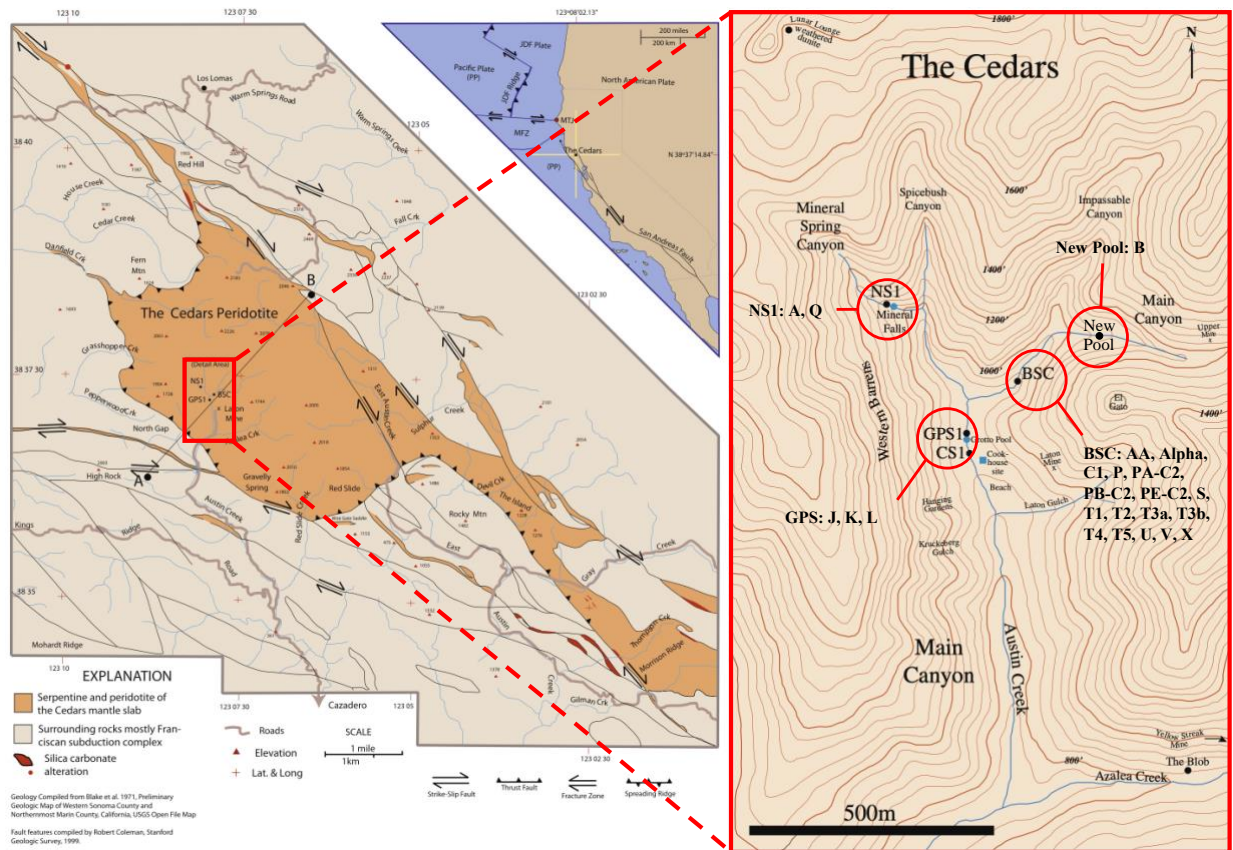
Figure 2. Map of The Cedars site showing the location of samples. Sample locations indicated in the right panel include NS1 (samples: A, Q,), Grotto Pool Springs (GPS) (samples: J, K, L), Barnes Spring Complex (BSC) (samples: AA, Alpha, C1, P, PA-C2, PB-C2, PE-C2, PE-C3, S, T1, T2, T3a, T3b, T4, T5, U, V, X), and New Pool (sample: B). The "Wedding Cake" is located at the NS1 location above the Mineral Falls. Modified from Morrill et al. (2013) and Christensen et al. (2021).

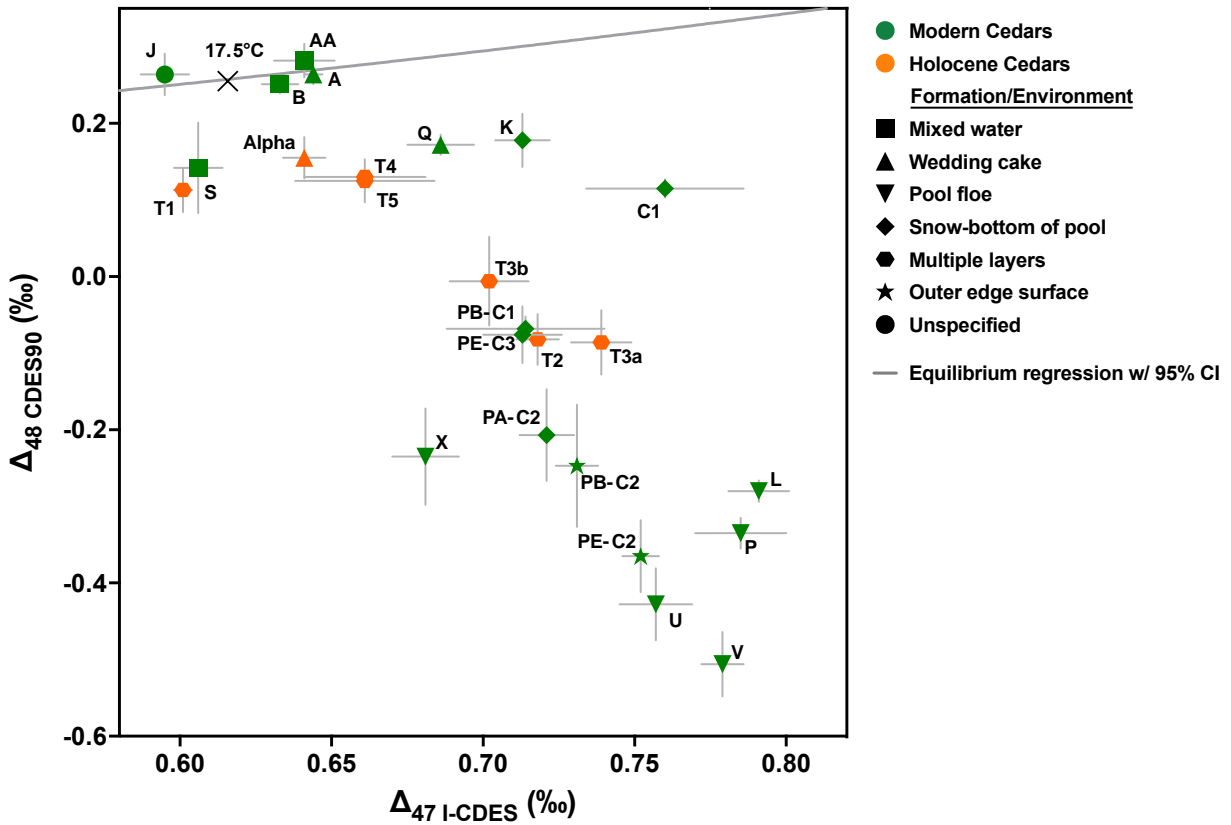**Figure 3.** The Δ_{47} and Δ_{48} values for modern (green symbols) and Holocene (orange symbols) carbonate mineral samples at The Cedars. Results are compared to equilibrium values (gray line) (Lucarelli et al., 2023), with the average water temperature at The Cedars of 17.5±1 °C (Morill et al., 2013; Christensen et al., 2021) indicated (X symbol). The samples that exhibit the largest KIEs were primarily recovered from surface floes (pool floe, downward triangles). The samples that are within error (±1 SE) of equilibrium are from areas where surface and spring waters mix (squares), 1 wedding cake sample (triangle), and 1 sample from the GPS location from an unspecified formation (circle). A linear regression through all samples indicates a slope of -3.223±0.519. Error bars indicate ±1 SE.

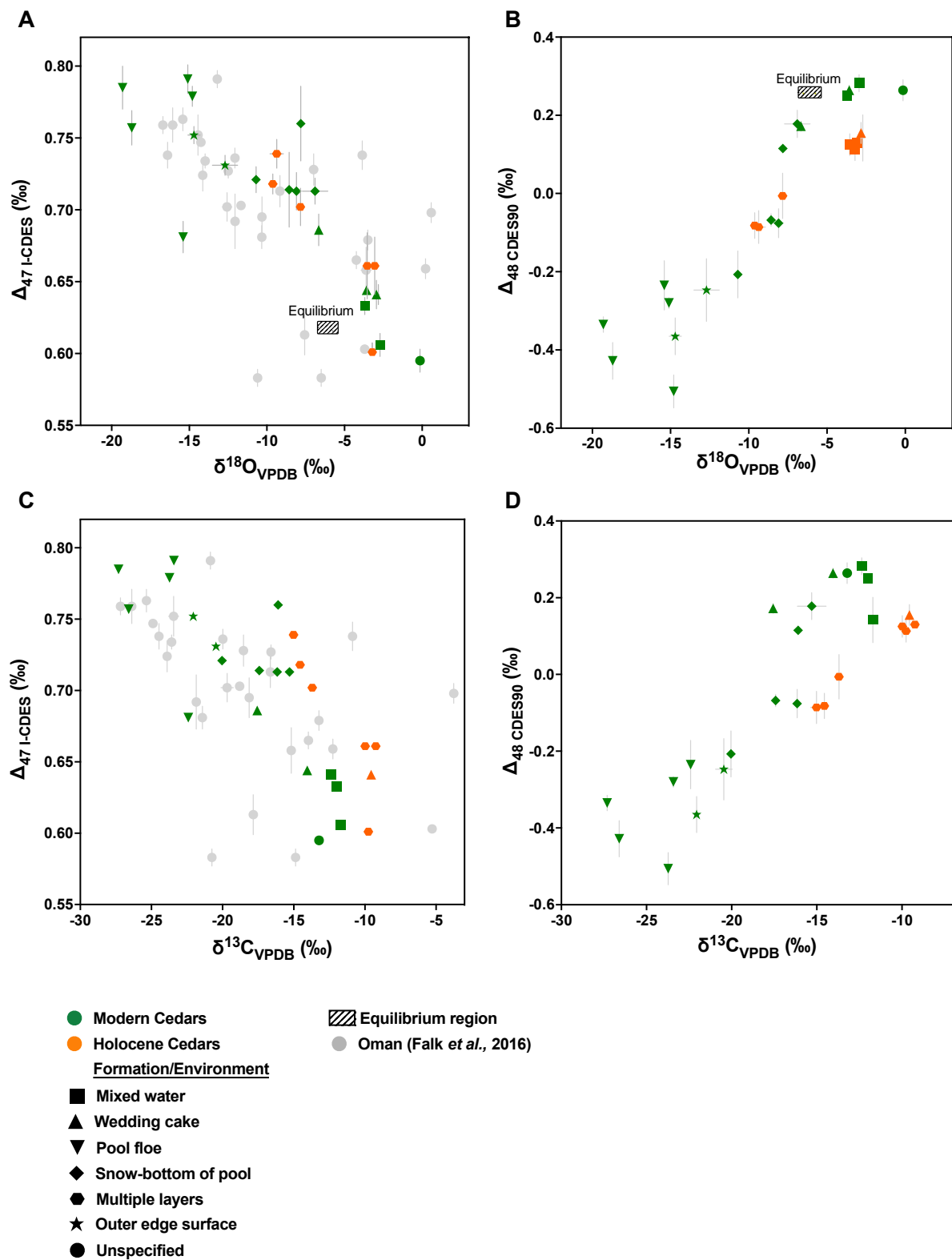**Figure 4.** Clumped isotope (Δ_{47}, Δ_{48}) versus bulk isotope ($\delta^{18}O$, $\delta^{13}C$) results of modern (green symbols) and Holocene (orange symbols) surface spring carbonate samples at The Cedars.

788 Results are compared to calculated equilibrium values (striped rectangle) (Kim and O'Neil,
789 1997; Kim et al., 2007; Dietzel et al., 2009; Lucarelli et al., 2023). Panels A and C include data
790 from carbonate veins precipitated from a peridotite body in Oman (gray cirlces) (Falk et al.,
791 2016). **A)** Δ_{47} versus $\delta^{18}O$ values for The Cedars and Oman (Falk et al., 2016). A linear
792 regression fit to The Cedars values yields a slope of -0.009±0.001, and a linear regression for the
793 Cedars and Oman values yields a slope of -0.007±0.001. **B)** Δ_{48} versus $\delta^{18}O$ values for The
794 Cedars. A linear regression fit to The Cedars values yields a slope of 0.041±0.003. **C)** Δ_{47} versus
795 $\delta^{13}C$ values for The Cedars and Oman (Falk et al., 2016). A linear regression fit to The Cedars
796 values yields a slope of -0.009±0.001, and a linear regression for to The Cedars and Oman values
797 yields a slope of -0.006±0.001. **D)** The Δ_{48} versus $\delta^{13}C$ values for The Cedars. A linear
798 regression yields a slope of 0.038±0.005. The Oman Δ_{47} values were published in the CDES 25
799 reference frame and converted to the CDES 90 reference frame (which is comparable to the I-
800 CDES reference frame used here) using an acid fractionation factor of 0.092‰ (Henkes et al.,
801 2013). Equilibrium values were calculated using the average water temperature at The Cedars of
802 17.5 ℃ (Morrill et al., 2013; Christiansen et al., 2021). Error bars indicate ±1 SE for clumped
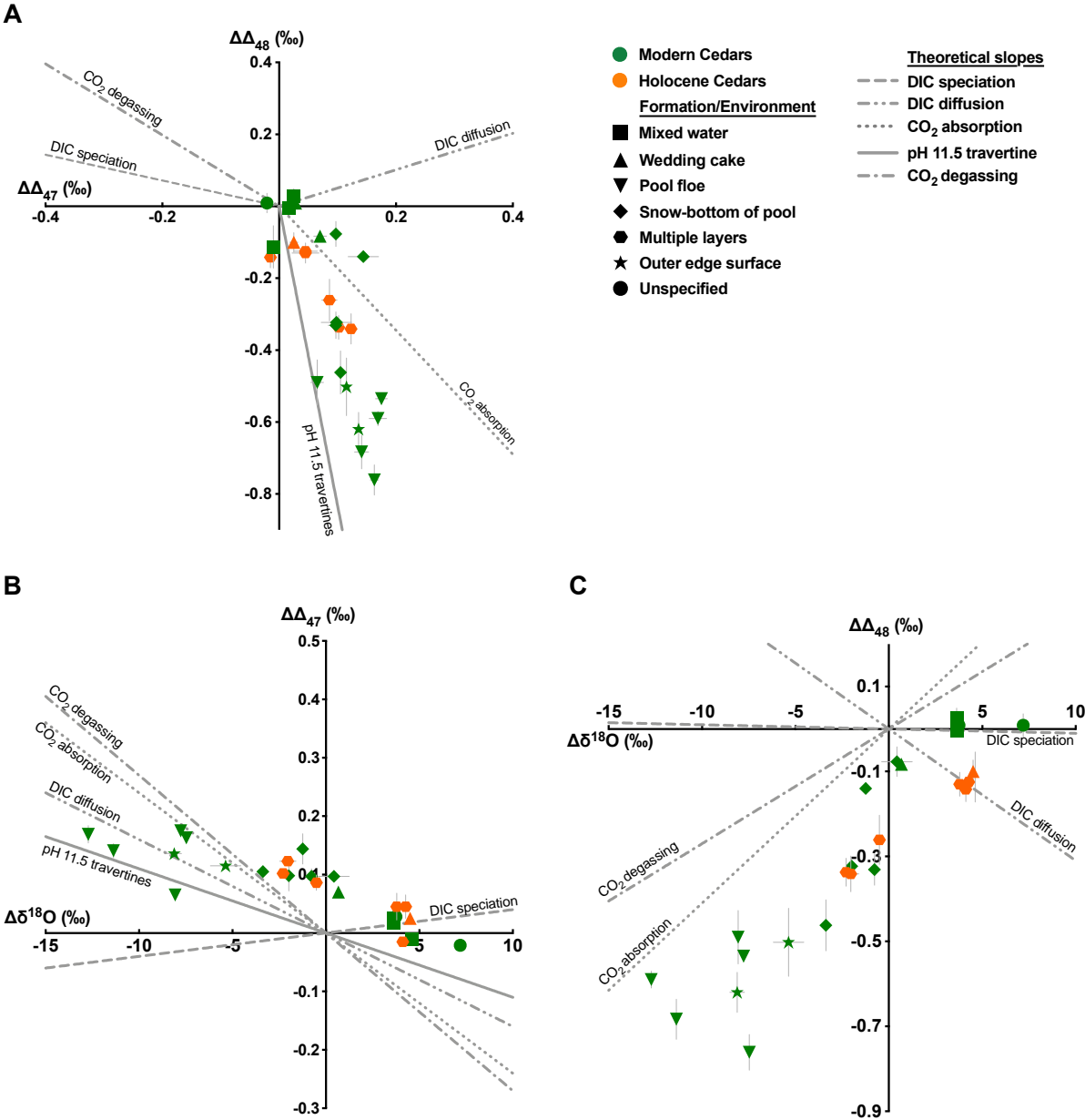803 isotope values and ±1 SD for bulk isotope values.
804
805
806
807
808
809
810
811
812
813
814
815
816
817
818

819

820
821
822 **Figure 5.** Extent of disequilibria in clumped (Δ_{47} and Δ_{48}) and oxygen isotope ($\delta^{18}O$) values in
823 the modern (green symbols) and Holocene (orange symbols) Cedars samples are shown with
824 theoretically predicted kinetic slopes from multiple processes (gray lines) (Guo, 2020). The
825 $\Delta\Delta_{47}$, $\Delta\Delta_{48}$, and $\Delta\delta^{18}O$ values were calculated by taking the difference between the measured
826 values and the calculated equilibrium values (Kim and O'Neil, 1997; Kim et al., 2007; Lucarelli
827 et al., 2023) for the average water temperature of The Cedars of 17.5 ºC (Morrill et al., 2013;
828 Christiansen et al., 2021). **A)** $\Delta\Delta_{48}$ versus $\Delta\Delta_{47}$ values, with a linear regression slope of -
829 3.223±0.519. **B)** $\Delta\Delta_{47}$ versus $\Delta\delta^{18}O$ values, with a linear regression slope of -0.009±0.001. **C)**
830 $\Delta\Delta_{48}$ versus $\Delta\delta^{18}O$ values, with a linear regression slope of 0.040±0.003. Error bars indicate ±1
831 SE for clumped isotope values and ±1 SD for bulk isotope values.
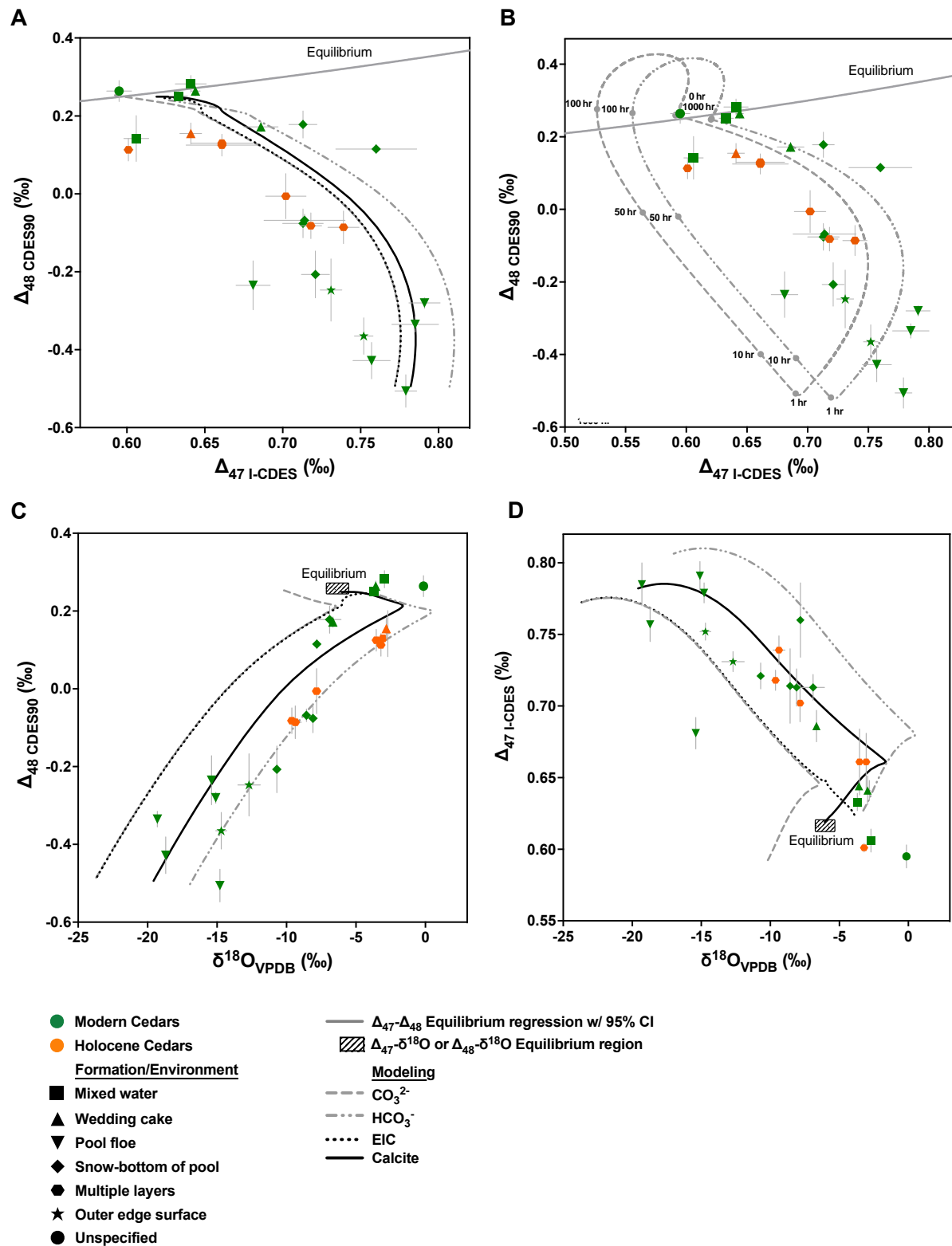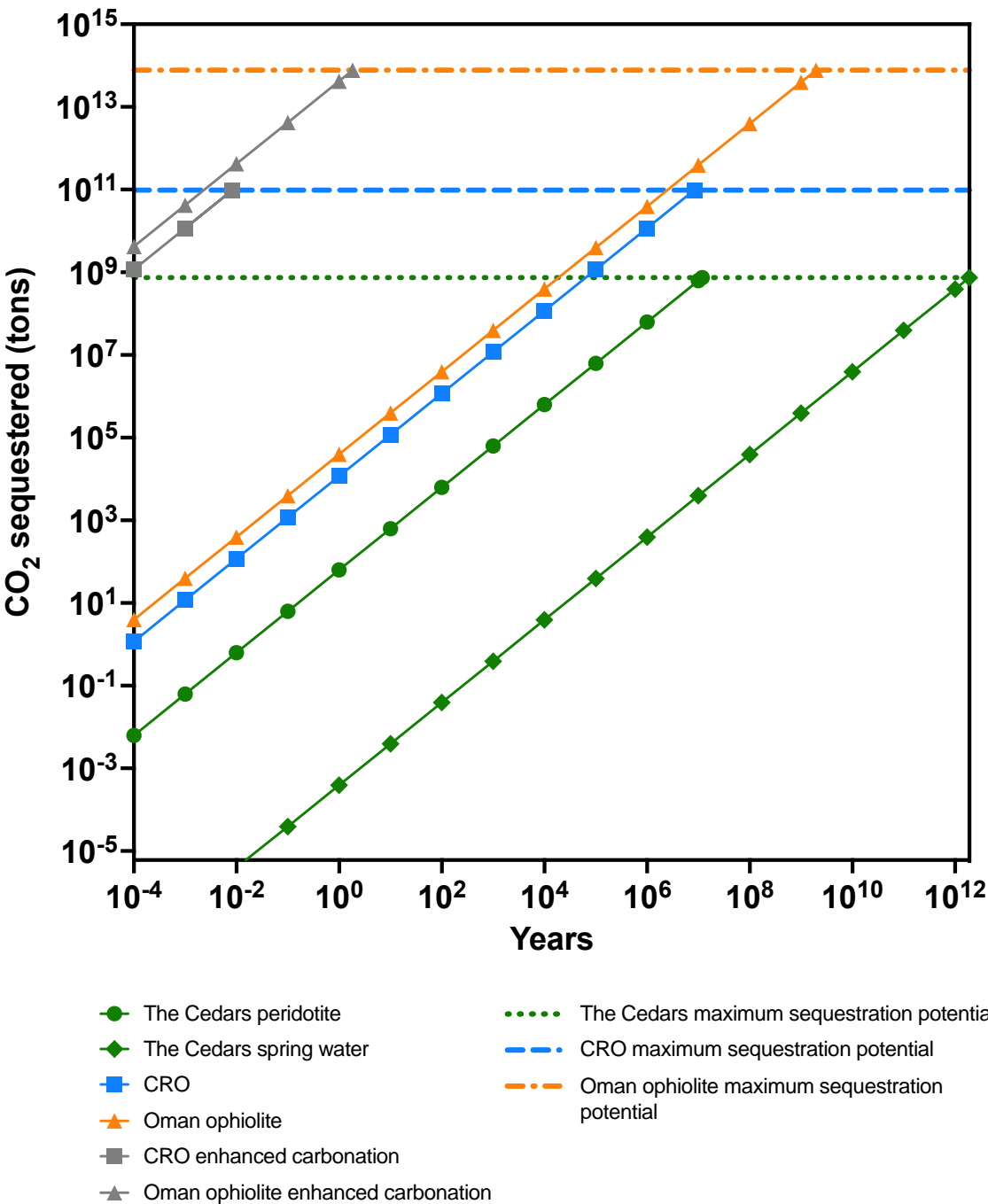832

Figure 6. The top four panels report measured Δ_{47}, Δ_{48}, and $\delta^{18}O$ values from the modern (green symbols) and Holocene (orange symbols) Cedars samples compared to model predictions (gray

837   and black curves) which were determined using code for the IsoDIC (Guo, 2020) and COAD

838   models (Watkins and Devriendt, 2021). Also shown are the calculated equilibrium values based

839   on the average water temperature at The Cedars of 17.5 $^{\circ}$C (gray line in panels A and B; striped

840   rectangle in panels C and D) (Kim and O'Neil, 1997; Kim et al., 2007; Morrill et al., 2013;

841   Christensen et al., 2021; Lucarelli et al., 2023). Panels E and F show the combined average Δ_{47}

842   and Δ_{48} values (red circles) from samples collected at the BSC locality (samples X, U, V), with

843   an apparent growth rate (R_p) of 4.8 x 10^{-7} to 8.0 x 10^{-7} mol m^{-2} s^{-1} (Christensen et al., 2021),

844   compared to COAD model predicted values (black curves). **A)** Measured Δ_{47} and Δ_{48} values

845   compared to IsoDIC model predicted values for HCO_3^- and CO_3^{-2} with the evolution time

846   indicated. **B)** Measured Δ_{47} and Δ_{48} values with COAD model predicted values for calcite, HCO_3^-

847   , CO_3^{-2}, and EIC. **C)** Measured Δ_{47} and $\delta^{18}O$ values with COAD model predicted values for

848   calcite, HCO_3^-, CO_3^{-2}, and EIC. **D)** Measured Δ_{48} and $\delta^{18}O$ values with COAD model predicted

849   values for calcite, HCO_3^-, CO_3^{-2}, and EIC. **E)** The measured and modeled Δ_{47} and $Log_{10}(R_p)$

850   values. The BSC average Δ_{47} value was determined to be 0.744±0.010‰. **F)** Measured and

851   modeled Δ_{48} and $Log_{10}(R_p)$ values. The BSC average Δ_{48} value was determined to be -

852   0.407±0.037‰. The IsoDIC and COAD models were based on the modern Cedars surface floe

853   conditions with the following input parameters: solution temperature of 17.5 ℃, solution pH

854   11.5, air pCO_2 of 400 ppm, air $\delta^{13}C_{VPDB}$ of -8.431‰, water $\delta^{18}O_{VPDB}$ of 36.3±0.6‰, taken as the

855   average of measurements from the NS1, GSP1, and BSC locations (Morrill et al., 2013). Error

856   bars indicate ±1 SE for clumped isotope values and ±1 SD for bulk isotope values.

857

858

859

Figure 7. Calculations of natural rates of CO_2 sequestration in The Cedars peridotite (green circles), spring water at the site (green diamonds), the Coastal Range Ophiolite (CRO; blue squares), and the Oman ophiolite (orange triangles). The estimated maximum CO_2 sequestration potential was calculated to be $\sim 7.4 \times 10^8$ tons for The Cedars (green dotted line), $\sim 9.7 \times 10^{10}$ tons for the CRO (Carnevale, 2013; blue dashed line), and $\sim 7.7 \times 10^{13}$ tons for the Oman ophiolite (Kelemen and Matter, 2008; orange dash-dot line). The rate of mineral formation in The Cedars springs was measured by Christensen et al. (2021) and constrained here with our dual clumped

861
862
863
864
865
866
867
868
869

870   isotope measurements and modeled carbonate mineralization rates. In addition, the CO_2
871   sequestered from enhanced *in situ* sequestration is shown for the CRO (gray squares) and the Oman
872   ophiolite (gray triangles), following methods from Kelemen and Matter (2008) for enhanced
873   geologic CO_2 sequestration in the Oman ophiolite of ~2×10^9 tons of CO_2 sequestered per year.
874   For natural carbonation, we estimate that the sequestration potentials at The Cedars, CRO, and
875   Oman ophiolite would be reached after ~8.2×10^6 years, ~8.3×10^6 years, and ~1.9×10^9 years,
876   respectively. For enhanced *in situ* carbonation, the maximum sequestration potential at the CRO
877   and Oman Ophiolite could be reached in <1 year. All calculated rates assume complete
878   consumption of Mg, Ca, and Fe in the respective formations (Kelemen and Matter, 2008; Matter
879   and Kelemen, 2009; Carnevale, 2013), and consider the ophiolite in Oman and the CRO to be ~30
880   % relict olivine (Kelemen and Matter, 2008; Carnevale, 2013). The peridotite in The Cedars is ~70
881   % relict olivine (Coleman, 2000; Blake et al., 2012; Morrill et al., 2013).
882

883 **Tables**
884

Sample Name	Sample Composition	Location	Notes
A	Travertine	NS1	Wedding Cake - Rim Formation
AA	Aragonite 91%; Calcite 1%; Brucite 8%	BSC	Mixed Water (BSC + Creek)
Alpha	Travertine	BSC	Wedding Cake - Rim Formation
B	Unspecified (Non-Travertine)	New Pool	Mixed Water (New Pool Spring + Creek)
C1	Aragonite 86%; Calcite 7%; Brucite 7%	BSC	Snow - Bottom of Pool
J	Unspecified (Non-Travertine)	GPS	Unspecified
K	Aragonite 25%; Calcite 20%; Hydromagnesite 50%; Nitromagnesite 2%; Nesquehonite 3%	GPS	Snow - Bottom of Pool
L	Unspecified (Non-Travertine)	GPS	Pool Floe
P	Aragonite 78%; Calcite 18%; Brucite 4%	BSC	Pool Floe
PA-C2	Unspecified (Non-Travertine)	BSC	Snow - Bottom of Pool
PB-C1	Aragonite 86%; Calcite 7%; Brucite 7%	BSC	Snow - Bottom of Pool
PB-C2	Aragonite 46%; Calcite 49%; Brucite 5%	BSC	Outer Edge Surface
PE-C2	Aragonite 78%; Calcite 18%; Brucite 4%	BSC	Outer Edge Surface
PE-C3	Unspecified (Non-Travertine)	BSC	Snow - Bottom of Pool
Q	Unspecified (Non-Travertine)	NS1	Wedding Cake - Floe
S	Unspecified (Non-Travertine)	BSC	Mixed Water (BSC + Creek)
T1	Travertine	BSC	Hand Sample - Multiple Layers
T2	Travertine	BSC	Hand Sample - Multiple Layers
T3a	Travertine	BSC	Hand Sample - Multiple Layers
T3b	Travertine	BSC	Hand Sample - Multiple Layers
T4	Travertine	BSC	Hand Sample - Multiple Layers
T5	Travertine	BSC	Hand Sample - Multiple Layers
U	Unspecified (Non-Travertine)	BSC	Pool Floe
V	Unspecified (Non-Travertine)	BSC	Pool Floe
X	Unspecified (Non-Travertine)	BSC	Pool Floe

885
886 **Table 1:** Sample information provided by Christensen et al. (2021).
887
888
889
890
891
892
893
894
895
896

Sample Name	Number of Replicates	δ¹³C VPDB (‰)	1 S.D.	δ¹⁸O VPDB (‰)	1 S.D.	Δδ¹⁸O (‰)	Δ₄₇ I-CDES (‰)	1 S.D.	1 S.E.	ΔΔ₄₇ (‰)	Δ₄₈ CDES90 (‰)	1 S.D.	1 S.E.	ΔΔ₄₈ (‰)
A	3	-14.1	0.0	-3.6	0.1	3.8	0.644	0.005	0.003	0.028	0.264	0.022	0.013	0.009
AA	6	-12.4	0.1	-3.0	0.1	3.6	0.641	0.024	0.010	0.025	0.282	0.054	0.022	0.027
Alpha	6	-9.6	0.1	-2.8	0.1	4.5	0.641	0.016	0.007	0.025	0.155	0.066	0.027	-0.100
B	3	-12.0	0.0	-3.7	0.0	3.6	0.633	0.010	0.006	0.017	0.251	0.021	0.012	-0.004
C1	4	-16.1	0.1	-7.8	0.2	-1.2	0.760	0.051	0.026	0.144	0.115	0.025	0.012	-0.140
J	4	-13.2	0.0	-0.1	0.2	7.2	0.595	0.015	0.008	-0.021	0.264	0.054	0.027	0.009
K	9	-15.3	0.8	-6.9	0.8	0.4	0.713	0.027	0.009	0.097	0.178	0.104	0.035	-0.077
L	4	-23.4	0.1	-15.1	0.1	-7.8	0.791	0.020	0.010	0.175	-0.280	0.027	0.014	-0.535
P	5	-27.3	0.0	-19.3	0.0	-12.7	0.785	0.033	0.015	0.169	-0.335	0.045	0.020	-0.590
PA-C2	5	-20.0	0.1	-10.7	0.2	-3.4	0.721	0.020	0.009	0.105	-0.207	0.134	0.060	-0.462
PB-C1	3	-17.4	0.0	-8.6	0.1	-2.0	0.714	0.045	0.026	0.098	-0.068	0.028	0.016	-0.323
PB-C2	5	-20.5	0.5	-12.7	0.8	-5.4	0.731	0.016	0.007	0.115	-0.247	0.180	0.080	-0.502
PE-C2	11	-22.1	0.2	-14.7	0.4	-8.1	0.752	0.021	0.006	0.136	-0.365	0.157	0.047	-0.620
PE-C3	8	-16.2	0.2	-8.1	0.3	-0.8	0.713	0.035	0.013	0.097	-0.076	0.105	0.037	-0.331
Q	5	-17.6	0.1	-6.7	0.1	0.7	0.686	0.025	0.011	0.070	0.172	0.029	0.013	-0.083
S	3	-11.7	0.0	-2.7	0.1	4.6	0.606	0.014	0.008	-0.010	0.142	0.102	0.059	-0.113
T1	6	-9.8	0.1	-3.2	0.2	4.1	0.601	0.007	0.003	-0.015	0.113	0.072	0.029	-0.142
T2	13	-14.6	0.2	-9.6	0.3	-2.3	0.718	0.024	0.007	0.102	-0.082	0.119	0.033	-0.337
T3a	13	-15.0	0.4	-9.4	0.4	-2.0	0.739	0.036	0.010	0.123	-0.086	0.153	0.042	-0.341
T3b	3	-13.7	0.2	-7.8	0.1	-0.5	0.702	0.023	0.013	0.086	-0.006	0.100	0.058	-0.261
T4	3	-10.0	0.1	-3.5	0.1	3.8	0.661	0.039	0.023	0.045	0.125	0.049	0.028	-0.130
T5	3	-9.2	0.0	-3.1	0.0	4.3	0.661	0.035	0.020	0.045	0.130	0.013	0.007	-0.125
U	5	-26.6	0.0	-18.7	0.1	-11.4	0.757	0.028	0.012	0.141	-0.428	0.104	0.047	-0.683
V	11	-23.7	0.1	-14.8	0.1	-7.5	0.779	0.023	0.007	0.163	-0.506	0.139	0.042	-0.761
X	7	-22.4	0.1	-15.4	0.1	-8.1	0.681	0.029	0.011	0.065	-0.235	0.167	0.063	-0.490

898

899 **Table 2:** Clumped and bulk isotopic values for all samples measured in this study. The

900 calculations to determine $\Delta\delta^{18}O$, $\Delta\Delta_{47}$, and $\Delta\Delta_{48}$ values were performed assuming equilibrium

901 values for the average temperature at The Cedars of 17.5 °C (Kim et al., 2007; Dietzel et al.,

902 2009; Morrill et al., 2013; Christensen et al., 2021; Lucarelli et al., 2023).

903

904 **References**

905 Affek H. P., Bar-Matthews M., Ayalon A., Matthews A. and Eiler J. M. (2008)
906   Glacial/interglacial temperature variations in Soreq cave speleothems as recorded by
907   'clumped isotope' thermometry. *Geochimica et Cosmochimica Acta* **72**, 5351–5360.

908 Anderson N. T., Kelson J. R., Kele S., Daëron M., Bonifacie M., Horita J., Mackey T. J., John C.
909   M., Kluge T., Petschnig P., Jost A. B., Huntington K. W., Bernasconi S. M. and

910 Bergmann K. D. (2021) A Unified Clumped Isotope Thermometer Calibration (0.5–
911   1,100°C) Using Carbonate-Based Standardization. *Geophysical Research Letters* **48**.

912 Bajnai D., Guo W., Spötl C., Coplen T. B., Methner K., Löffler N., Krsnik E., Gischler E.,
913   Hansen M., Henkel D., Price G. D., Raddatz J., Scholz D. and Fiebig J. (2020) Dual
914   clumped isotope thermometry resolves kinetic biases in carbonate formation
915   temperatures. *Nature Communications* **11**, 4005.

916 Barnes I. and O'Neil J. R. (1969) The Relationship between Fluids in Some Fresh Alpine-Type
917   Ultramafics and Possible Modern Serpentinization, Western United States. *Geol Soc*
918   *America Bull* **80**, 1947.

919 Beck W. C., Grossman E. L. and Morse J. W. (2005) Experimental studies of oxygen isotope
920   fractionation in the carbonic acid system at 15°, 25°, and 40°C. *Geochimica et*
921   *Cosmochimica Acta* **69**, 3493–3503.

922 Bernasconi S. M., Daëron M., Bergmann K. D., Bonifacie M., Meckler A. N., Affek H. P.,
923   Anderson N., Bajnai D., Barkan E., Beverly E., Blamart D., Burgener L., Calmels D.,
924   Chaduteau C., Clog M., Davidheiser-Kroll B., Davies A., Dux F., Eiler J., Elliott B.,
925   Fetrow A. C., Fiebig J., Goldberg S., Hermoso M., Huntington K. W., Hyland E., Ingalls
926   M., Jaggi M., John C. M., Jost A. B., Katz S., Kelson J., Kluge T., Kocken I. J., Laskar
927   A., Leutert T. J., Liang D., Lucarelli J., Mackey T. J., Mangenot X., Meinicke N.,
928   Modestou S. E., Müller I. A., Murray S., Neary A., Packard N., Passey B. H., Pelletier E.,
929   Petersen S., Piasecki A., Schauer A., Snell K. E., Swart P. K., Tripati A., Upadhyay D.,
930   Vennemann T., Winkelstern I., Yarian D., Yoshida N., Zhang N. and Ziegler M. (2021)
931   InterCarb: A Community Effort to Improve Interlaboratory Standardization of the
932   Carbonate Clumped Isotope Thermometer Using Carbonate Standards. *Geochem*
933   *Geophys Geosyst* **22**.

934 Bernasconi S. M., Müller I. A., Bergmann K. D., Breitenbach S. F. M., Fernandez A., Hodell D.
935   A., Jaggi M., Meckler A. N., Millan I. and Ziegler M. (2018) Reducing Uncertainties in
936   Carbonate Clumped Isotope Analysis Through Consistent Carbonate-Based
937   Standardization. *Geochem. Geophys. Geosyst.* **19**, 2895–2914.

938 Blake M. C., Bailey E. H. and Wentworth C. M. (2012) The Cedars Ultramafic Mass, Sonoma
939   County, California. *USGS Open-File Report* **2012–1164**, 1–16.

940 Brand W. A., Assonov S. S. and Coplen T. B. (2010) Correction for the 17O interference in
941   δ(13C) measurements when analyzing CO2 with stable isotope mass spectrometry
942   (IUPAC Technical Report). *Pure and Applied Chemistry* **82**, 1719–1733.

943 Bruni J., Canepa M., Chiodini G., Cioni R., Cipolli F., Longinelli A., Marini L., Ottonello G. and
944   Vetuschi Zuccolini M. (2002) Irreversible water-rock mass transfer accompanying the
945   generation of the neutral, Mg-HCO3 and high-pH, Ca-OC spring waters of the Genova
946   province, Italy. *Applied Geochemistry* **17**, 455–474.

947 Carnevale D. C. (2013) *Carbon sequestration potential of the Coast Range Ophiolite in*
948   *California*., University of Rhode Island ProQuest Dissertations Publishing.

Chen S., Gagnon A. C. and Adkins J. F. (2018) Carbonic anhydrase, coral calcification and a new model of stable isotope vital effects. *Geochimica et Cosmochimica Acta* **236**, 179–197.

Christensen J. N., Watkins J. M., Devriendt L. S., DePaolo D. J., Conrad M. E., Voltolini M., Yang W. and Dong W. (2021) Isotopic fractionation accompanying CO2 hydroxylation and carbonate precipitation from high pH waters at The Cedars, California, USA. *Geochimica et Cosmochimica Acta* **301**, 91–115.

Cipolli F., Gambardella B., Marini L., Ottonello G. and Vetuschi Zuccolini M. (2004) Geochemistry of high-pH waters from serpentinites of the Gruppo di Voltri (Genova, Italy) and reaction path modeling of CO2 sequestration in serpentinite aquifers. *Applied Geochemistry* **19**, 787–802.

Coleman R. G. (2004) Geologic Nature of the Jasper Ridge Biological Preserve, San Francisco Peninsula, California. *International Geology Review* **46**, 629–637.

Coleman R. G. (2000) Prospecting for ophiolites along the California continental margin. In *Ophiolites and oceanic crust: new insights from field studies and the Ocean Drilling Program* Geological Society of America.

Daëron M., Blamart D., Peral M. and Affek H. P. (2016) Absolute isotopic abundance ratios and the accuracy of Δ47 measurements. *Chemical Geology* **442**, 83–96.

Defliese W. F. and Lohmann K. C. (2015) Non-linear mixing effects on mass-47 CO $_2$ clumped isotope thermometry: Patterns and implications: Non-linear mixing effects on mass-47 clumped isotopes. *Rapid Commun. Mass Spectrom.* **29**, 901–909.

Dennis K. J., Affek H. P., Passey B. H., Schrag D. P. and Eiler J. M. (2011) Defining an absolute reference frame for 'clumped' isotope studies of CO2. *Geochimica et Cosmochimica Acta* **75**, 7117–7131.

Devriendt L. S., Watkins J. M. and McGregor H. V. (2017) Oxygen isotope fractionation in the CaCO3-DIC-H2O system. *Geochimica et Cosmochimica Acta* **214**, 115–142.

Dietzel M., Tang J., Leis A. and Köhler S. J. (2009) Oxygen isotopic fractionation during inorganic calcite precipitation ― Effects of temperature, precipitation rate and pH. *Chemical Geology* **268**, 107–115.

Drohan P. J. and Brittingham M. (2012) Topographic and Soil Constraints to Shale-Gas Development in the Northcentral Appalachians. *Soil Science Society of America Journal* **76**, 1696–1706.

Eiler J. M. (2007) "Clumped-isotope" geochemistry—The study of naturally-occurring, multiply-substituted isotopologues. *Earth and Planetary Science Letters* **262**, 309–327.

Eiler J. M. and Schauble E. (2004) 18O13C16O in Earth's atmosphere. *Geochimica et Cosmochimica Acta* **68**, 4767–4777.

985 Falk E. S., Guo W., Paukert A. N., Matter J. M., Mervine E. M. and Kelemen P. B. (2016)
986   Controls on the stable isotope compositions of travertine from hyperalkaline springs in
987   Oman: Insights from clumped isotope measurements. *Geochimica et Cosmochimica Acta*
988   **192**, 1–28.

989 Fiebig J., Bajnai D., Löffler N., Methner K., Krsnik E., Mulch A. and Hofmann S. (2019)
990   Combined high-precision Δ48 and Δ47 analysis of carbonates. *Chemical Geology* **522**,
991   186–191.

992 Fiebig J., Daëron M., Bernecker M., Guo W., Schneider G., Boch R., Bernasconi S. M., Jautzy J.
993   and Dietzel M. (2021) Calibration of the dual clumped isotope thermometer for
994   carbonates. *Geochimica et Cosmochimica Acta*, S0016703721004208.

995 García del Real P., Maher K., Kluge T., Bird D. K., Brown G. E. and John C. M. (2016)
996   Clumped-isotope thermometry of magnesium carbonates in ultramafic rocks. *Geochimica*
997   *et Cosmochimica Acta* **193**, 222–250.

998 Ghosh P., Adkins J., Affek H., Balta B., Guo W., Schauble E. A., Schrag D. and Eiler J. M.
999   (2006) 13C–18O bonds in carbonate minerals: A new kind of paleothermometer.
1000   *Geochimica et Cosmochimica Acta* **70**, 1439–1456.

1001 Guo W. (2020) Kinetic clumped isotope fractionation in the DIC-H2O-CO2 system: Patterns,
1002   controls, and implications. *Geochimica et Cosmochimica Acta* **268**, 230–257.

1003 Guo W., Mosenfelder J. L., Goddard W. A. and Eiler J. M. (2009) Isotopic fractionations
1004   associated with phosphoric acid digestion of carbonate minerals: Insights from first-
1005   principles theoretical modeling and clumped isotope measurements. *Geochimica et*
1006   *Cosmochimica Acta* **73**, 7203–7225.

1007 Guo W. and Zhou C. (2019) Patterns and controls of disequilibrium isotope effects in
1008   speleothems: Insights from an isotope-enabled diffusion-reaction model and implications
1009   for quantitative thermometry. *Geochimica et Cosmochimica Acta* **267**, 196–226.

1010 Hendy C. H. (1971) The isotopic geochemistry of speleothems—I. The calculation of the effects
1011   of different modes of formation on the isotopic composition of speleothems and their
1012   applicability as palaeoclimatic indicators. *Geochimica et Cosmochimica Acta* **35**, 801–
1013   824.

1014 Henkes G. A., Passey B. H., Wanamaker A. D., Grossman E. L., Ambrose W. G. and Carroll M.
1015   L. (2013) Carbonate clumped isotope compositions of modern marine mollusk and
1016   brachiopod shells. *Geochimica et Cosmochimica Acta* **106**, 307–325.

1017 Hill P. S., Schauble E. A. and Tripati A. (2020) Theoretical constraints on the effects of added
1018   cations on clumped, oxygen, and carbon isotope signatures of dissolved inorganic carbon
1019   species and minerals. *Geochimica et Cosmochimica Acta* **269**, 496–539.

1020 Hill P. S., Tripati A. K. and Schauble E. A. (2014) Theoretical constraints on the effects of pH,
1021   salinity, and temperature on clumped isotope signatures of dissolved inorganic carbon

1022   species and precipitating carbonate minerals. *Geochimica et Cosmochimica Acta* **125**,
1023   610–652.

1024 Holzman D. C. (2011) Methane Found in Well Water Near Fracking Sites. *Environ Health*
1025   *Perspect* **119**.

1026 John C. M. and Bowen D. (2016) Community software for challenging isotope analysis: First
1027   applications of 'Easotope' to clumped isotopes: Community software for challenging
1028   isotope analysis. *Rapid Commun. Mass Spectrom.* **30**, 2285–2300.

1029 Kastrinakis A., Skliros V., Tsakiridis P. and Perraki M. (2021) CO2-Mineralised Nesquehonite:
1030   A New "Green" Building Material. In *International Conference on Raw Materials and*
1031   *Circular Economy* RawMat 2021. MDPI. p. 60.

1032 Kelemen P. B., Godard M., Johnson K. T. M., Okazaki K., Manning C. E., Urai J. L.,
1033   Michibayashi K., Harris M., A. Coggon. J. and Teagle D. A. H. (2017) Peridotite
1034   carbonation at the leading edge of the mantle wedge: OmDP Site BT1. *American*
1035   *Geophysical Union*.

1036 Kelemen P. B. and Matter J. (2008) In situ carbonation of peridotite for CO_2 storage. *Proc. Natl.*
1037   *Acad. Sci. U.S.A.* **105**, 17295–17300.

1038 Kelemen P. B., Matter J., Streit E. E., Rudge J. F., Curry W. B. and Blusztajn J. (2011) Rates and
1039   Mechanisms of Mineral Carbonation in Peridotite: Natural Processes and Recipes for
1040   Enhanced, in situ CO_2 Capture and Storage. *Annu. Rev. Earth Planet. Sci.* **39**, 545–576.

1041 Kim S. T. and O'Neil J. R. (1997) Equilibrium and nonequilibrium oxygen isotope effects in
1042   synthetic carbonates. *Geochimica et Cosmochimica Acta* **61**, 3461–3475.

1043 Kim S.-T., O'Neil J. R., Hillaire-Marcel C. and Mucci A. (2007) Oxygen isotope fractionation
1044   between synthetic aragonite and water: Influence of temperature and Mg2+
1045   concentration. *Geochimica et Cosmochimica Acta* **71**, 4704–4715.

1046 Kiviat E. (2013) Risks to biodiversity from hydraulic fracturing for natural gas in the Marcellus
1047   and Utica shales: Hydraulic fracturing and biodiversity. *Ann. N.Y. Acad. Sci.* **1286**, 1–14.

1048 Lerman A. and Stumm W. (1989) CO2 storage and alkalinity trends in lakes. *Water Research* **23**,
1049   139–146.

1050 Liu Z., Deng Z., Davis S. J., Giron C. and Ciais P. (2022) Monitoring global carbon emissions in
1051   2021. *Nat Rev Earth Environ* **3**, 217–219.

1052 Lívanský K. (1982) Effect of temperature and pH on absorption of carbon dioxide by a free level
1053   of mixed solutions of some buffers. *Folia Microbiol* **27**, 55–59.

1054 Lucarelli J. K., Carroll H. M., Ulrich R. N., Elliott B. M., Coplen T. B., Eagle R. A. and Tripati
1055   A. (2023) Equilibrated Gas and Carbonate Standard-Derived Dual (Δ_{47} and Δ_{48}) Clumped
1056   Isotope Values. *Geochem Geophys Geosyst* **24**.

1057 Matter J. M. and Kelemen P. B. (2009) Permanent storage of carbon dioxide in geological
1058   reservoirs by mineral carbonation. *Nature Geosci* **2**, 837–841.

1059 McConnaughey T. (1989) 13C and 18O isotopic disequilibrium in biological carbonates: II. In
1060   vitro simulation of kinetic isotope effects. *Geochimica et Cosmochimica Acta* **53**, 163–
1061   171.

1062 McDermott F., Atkinson T. C., Fairchild I. J., Baldini L. M. and Mattey D. P. (2011) A first
1063   evaluation of the spatial gradients in δ18O recorded by European Holocene speleothems.
1064   *Global and Planetary Change* **79**, 275–287.

1065 Moody J. B. (1976) Serpentinization: a review. *Lithos* **9**, 125–138.

1066 Morrill P. L., Kuenen J. G., Johnson O. J., Suzuki S., Rietze A., Sessions A. L., Fogel M. L. and
1067   Nealson K. H. (2013) Geochemistry and geobiology of a present-day serpentinization site
1068   in California: The Cedars. *Geochimica et Cosmochimica Acta* **109**, 222–240.

1069 de Obeso J. C. and Kelemen P. B. (2018) Fluid rock interactions on residual mantle peridotites
1070   overlain by shallow oceanic limestones: Insights from Wadi Fins, Sultanate of Oman.
1071   *Chemical Geology* **498**, 139–149.

1072 Passey B. H., Levin N. E., Cerling T. E., Brown F. H. and Eiler J. M. (2010) High-temperature
1073   environments of human evolution in East Africa based on bond ordering in paleosol
1074   carbonates. *Proceedings of the National Academy of Sciences* **107**, 11245–11249.

1075 Power I. M., Wilson S. A. and Dipple G. M. (2013) Serpentinite Carbonation for CO2
1076   Sequestration. *Elements* **9**, 115–121.

1077 Power I. M., Wilson S. A., Small D. P., Dipple G. M., Wan W. and Southam G. (2011)
1078   Microbially Mediated Mineral Carbonation: Roles of Phototrophy and Heterotrophy.
1079   *Environ. Sci. Technol.* **45**, 9061–9068.

1080 Saenger C., Affek H. P., Felis T., Thiagarajan N., Lough J. M. and Holcomb M. (2012)
1081   Carbonate clumped isotope variability in shallow water corals: Temperature dependence
1082   and growth-related vital effects. *Geochimica et Cosmochimica Acta* **99**, 224–242.

1083 Schauble E. A., Ghosh P. and Eiler J. M. (2006) Preferential formation of 13C–18O bonds in
1084   carbonate minerals, estimated using first-principles lattice dynamics. *Geochimica et*
1085   *Cosmochimica Acta* **70**, 2510–2529.

1086 Schefer J. and Grube M. (1995) Low temperature structure of magnesium nitrate hexahydrate,
1087   Mg (NO3)2·6H2O: A neutron diffraction study at 173 K. *Materials Research Bulletin* **30**,
1088   1235–1241.

1089 Sleep N. H., Meibom A., Fridriksson Th., Coleman R. G. and Bird D. K. (2004) H 2 -rich fluids
1090   from serpentinization: Geochemical and biotic implications. *Proc. Natl. Acad. Sci. U.S.A.*
1091   **101**, 12818–12823.

1092 Spooner P. T., Guo W., Robinson L. F., Thiagarajan N., Hendry K. R., Rosenheim B. E. and
1093   Leng M. J. (2016) Clumped isotope composition of cold-water corals: A role for vital
1094   effects? *Geochimica et Cosmochimica Acta* **179**, 123–141.

1095 Suzuki S., Ishii S., Hoshino T., Rietze A., Tenney A., Morrill P. L., Inagaki F., Kuenen J. G. and
1096   Nealson K. H. (2017) Unusual metabolic diversity of hyperalkaliphilic microbial
1097   communities associated with subterranean serpentinization at the Cedars. *ISME Journal*
1098   **11**, 2584–2598.

1099 Swart P. K., Lu C., Moore E. W., Smith M. E., Murray S. T. and Staudigel P. T. (2021) A
1100   calibration equation between Δ_{48} values of carbonate and temperature. *Rapid Commun*
1101   *Mass Spectrom* **35**.

1102 Tang J., Dietzel M., Fernandez A., Tripati A. K. and Rosenheim B. E. (2014) Evaluation of
1103   kinetic effects on clumped isotope fractionation ($\Delta 47$) during inorganic calcite
1104   precipitation. *Geochimica et Cosmochimica Acta* **134**, 120–136.

1105 Thiagarajan N., Adkins J. and Eiler J. (2011) Carbonate clumped isotope thermometry of deep-
1106   sea corals and implications for vital effects. *Geochimica et Cosmochimica Acta* **75**, 4416–
1107   4425.

1108 Tripati A. K., Hill P. S., Eagle R. A., Mosenfelder J. L., Tang J., Schauble E. A., Eiler J. M.,
1109   Zeebe R. E., Uchikawa J., Coplen T. B., Ries J. B. and Henry D. (2015) Beyond
1110   temperature: Clumped isotope signatures in dissolved inorganic carbon species and the
1111   influence of solution chemistry on carbonate mineral composition. *Geochimica et*
1112   *Cosmochimica Acta* **166**, 344–371.

1113 Uchikawa J., Chen S., Eiler J. M., Adkins J. F. and Zeebe R. E. (2021) Trajectory and timescale
1114   of oxygen and clumped isotope equilibration in the dissolved carbonate system under
1115   normal and enzymatically-catalyzed conditions at 25 °C. *Geochimica et Cosmochimica*
1116   *Acta* **314**, 313–333.

1117 Uchikawa J. and Zeebe R. E. (2012) The effect of carbonic anhydrase on the kinetics and
1118   equilibrium of the oxygen isotope exchange in the CO_2–H_2O system: Implications for
1119 $\delta 18O$ vital effects in biogenic carbonates. *Geochimica et Cosmochimica Acta* **95**, 15–34.

1120 UNITED NATIONS ENVIRONMENT PROGRAMME (2019) *EMISSIONS GAP REPORT*
1121   *2018.*, UNEP.

1122 Upadhyay D., Lucarelli J., Arnold A., Flores R., Bricker H., Ulrich R. N., Jesmok G., Santi L.,
1123   Defliese W., Eagle R. A., Carroll H. M., Bateman J. B., Petryshyn V., Loyd S. J., Tang J.,
1124   Priyadarshi A., Elliott B. and Tripati A. (2021) Carbonate clumped isotope analysis ($\Delta 47$)
1125   of 21 carbonate standards determined via gas-source isotope-ratio mass spectrometry on
1126   four instrumental configurations using carbonate-based standardization and multiyear
1127   data sets. *Rapid Commun Mass Spectrom* **35**.

1128 Usdowski E., Michaelis J., Boettcher M. and Hoefs J. (1991) Factors for the oxygen isotope
1129   equilibrium fractionation between aqueous and gaseous CO_2, carbonic acid, bicarbonate,

carbonate, and water (19°C). *Zeitschrift fur physikalische chemie-international journal of research in physical chemistry & Chemical Physics* **170**, 237–249.

Watkins J. and Devriendt L. (2021) A generalizable box model for kinetic clumped isotope effects in the CaCO3 -DIC-H2O system., *Geochem. Geophys. Geosystems.*

Watkins J. M. and Hunt J. D. (2015) A process-based model for non-equilibrium clumped isotope effects in carbonates. *Earth and Planetary Science Letters* **432**, 152–165.

Weise A. and Kluge T. (2020) Isotope exchange rates in dissolved inorganic carbon between 40 °C and 90 °C. *Geochimica et Cosmochimica Acta* **268**, 56–72.

Yumol L. M., Uchikawa J. and Zeebe R. E. (2020) Kinetic isotope effects during CO2 hydration: Experimental results for carbon and oxygen fractionation. *Geochimica et Cosmochimica Acta* **279**, 189–203.

Zeebe R. E. (2020) Oxygen isotope fractionation between water and the aqueous hydroxide ion. *Geochimica et Cosmochimica Acta* **289**, 182–195.

Zedef V., Russell M. J., Fallick A. E. and Hall A. J. (2000) Genesis of Vein Stockwork and Sedimentary Magnesite and Hydromagnesite Deposits in the Ultramafic Terranes of Southwestern Turkey: A Stable Isotope Study. *Economic Geology* **95**, 429–445.

Zeebe R. E. and Wolf-Gladrow D. A. (2001) *CO₂ in seawater: equilibrium, kinetics, isotopes.*, Elsevier, Amsterdam ; New York.

Zhang J., Quay P. D. and Wilbur D. O. (1995) Carbon isotope fractionation during gas-water exchange and dissolution of CO2. *Geochimica et Cosmochimica Acta* **59**, 107–114.